

MAGPIS: A MULTI-ARRAY GALACTIC PLANE IMAGING SURVEY

DAVID J. HELFAND¹, ROBERT H. BECKER^{2,3}, RICHARD L. WHITE⁴, ADAM FALLON¹, & SARAH TUTTLE¹

Submitted to the Astronomical Journal

ABSTRACT

We present the Multi-Array Galactic Plane Imaging Survey (MAGPIS), which maps portions of the first Galactic quadrant with an angular resolution, sensitivity and dynamic range that surpasses existing radio images of the Milky Way by more than an order of magnitude. The source detection threshold at 20 cm is in the range 1-2 mJy over the 85% of the survey region ($5^\circ < l < 32^\circ$, $|b| < 0.8^\circ$) not covered by bright extended emission. We catalog over 3000 discrete sources (diameters mostly $< 30''$) and present an atlas of ~ 400 diffuse emission regions. New and archival data at 90 cm for the whole survey area are also presented. Comparison of our catalogs and images with the MSX mid-infrared data allow us to provide preliminary discrimination between thermal and non-thermal sources. We identify 49 high-probability supernova remnant candidates, increasing by a factor of seven the number of known remnants with diameters smaller than $5'$ in the survey region; several are pulsar wind nebula candidates and/or very small diameter remnants ($D < 45''$). We report the tentative identification of several hundred H II regions based on a comparison with the mid-IR data; they range in size from unresolved ultra-compact sources to large complexes of diffuse emission on scales of half a degree. In several of the latter regions, cospatial nonthermal emission illustrates the interplay between stellar death and birth. We comment briefly on plans for followup observations and our extension of the survey; when complemented by data from ongoing X-ray and mid-IR observations, we expect MAGPIS to provide the most complete census yet obtained of the birth and death of massive stars in the Milky Way.

Subject headings: surveys — catalogs — Galaxy: general — radio continuum: ISM — supernova remnants — HII regions

1. INTRODUCTION

The Milky Way is a galaxy of stars radiating most of their energy at optical wavelengths. But from stellar birth to stellar death, from the vast reaches of interstellar space to the tiniest of stellar corpses, radio and X-ray observations provide crucial diagnostics in our quest to understand the structure and evolution of our Galaxy and its denizens. These two spectral regimes are particularly crucial for studying massive stars: throughout their lives, stellar Lyman continuum photons produce H II regions with their associated free-free radio emission, while stellar wind shocks produce X-rays; in death, the remnants of supernovae are the brightest radio and X-ray sources in the Galaxy. Furthermore, the Galaxy is largely transparent in the radio and hard X-ray bands, giving us an unobstructed view through the plane, even at $b = 0^\circ$. We are in the process of conducting a large-scale survey of the Galactic plane at X-ray wavelengths with XMM, the first results of which have been reported elsewhere (Hands et al. 2004). Here we describe a complementary effort to provide a new, high-resolution, high-sensitivity view of centimetric radio emission in the Milky Way.

While significant progress has been made recently in surveying the extragalactic radio sky (*e.g.*, NVSS, SUMSS, and FIRST), the Galactic plane still remains inadequately explored. Even though the NVSS (Condon et al. 1998) covered the plane, it did so in snapshot mode with *uv* coverage insufficient to achieve high dynamic range (typical values achieved are $\sim 30:1$). The Canadian Galactic Plane Survey project (English et al. 1998) is covering a large region of the plane in the

second quadrant with better dynamic range, but with a resolution of only $65''$ and limited sensitivity in the continuum. The third and fourth Galactic quadrants are being surveyed using Parkes and the Australia Compact Telescope Array in the Southern Galactic Plane Survey (McClure-Griffiths et al. 2001), although the angular resolution is only $\sim 2'$ and the 5σ detection threshold is ~ 35 mJy in the continuum.

Fifteen years ago, we used observations originally taken by Dicke et al. (unpublished) in the B-configuration of the Very Large Array⁵ (supplemented by additional 20 cm and 6 cm time awarded to us) to produce a catalog of over 4000 compact sources within a degree of the plane in the longitude range $-20^\circ < l < 120^\circ$ (Becker et al. 1990; Zoonematkermani et al. 1990; White, Becker, and Helfand 1991; Helfand et al. 1992). Although the original analysis provided maps that were complete only to ~ 20 mJy at 20 cm, this remains the highest resolution and most sensitive census of compact sources over a large segment of the Galaxy. Comparison with the IRAS survey led us to identify more than 450 ultracompact H II regions, over 100 new planetary nebulae (which fill in the gap near $b = 0$ caused by extinction in optical searches – Kistiakowsky and Helfand 1995), and, along with 90 cm maps we obtained covering a small portion of the longitude range, more than a dozen new supernova remnant candidates.

Motivated by the torrent of new, high-resolution mid-infrared data from the GLIMPSE Legacy survey with Spitzer (Benjamin et al. 2003) and taking advantage of modern data analysis algorithms developed for our FIRST survey (Becker, White & Helfand 1995; White et al. 1997), we have recently completed a reanalysis of all of the existing snapshot data (over 3000 individual pointings including some new data de-

Electronic address: djh@astro.columbia.edu

¹ Dept. of Astronomy, Columbia University, New York, NY 10027

² Physics Dept., University of California, Davis, CA 95616

³ IGPP/Lawrence Livermore National Laboratory

⁴ Space Telescope Science Institute, Baltimore, MD 21218

⁵ The VLA is a facility of the National Radio Astronomy Observatory which is operated by Associated Universities, Inc. under cooperative agreement with the National Science Foundation.

signed to fill holes and improve quality in poorly covered regions). This work yielded 6 and 20 cm catalogs with over 6000 entries and flux density thresholds nearly a factor of two below those of the original analysis (White, Becker & Helfand 2005). Nonetheless, the single-configuration, snapshot nature of these observations renders the data problematic for all but the most compact radio sources in the plane.

A high-sensitivity, high-resolution, high-dynamic-range map of the radio continuum emission from the Galactic plane is now possible with a relatively modest investment of telescope time owing to advances in the VLA receivers over the last decade, the implementation of the highly efficient "survey mode" slewing algorithm, and improvements to the AIPS software package. We have begun to make this possibility a reality by producing a $5''$ -resolution image of 27 degrees of Galactic longitude in the first quadrant. Our plan over the coming several years is to extend this survey over the entire Spitzer GLIMPSE longitude range in the north, covering $5^\circ < l < 65^\circ$. This Multi-Array Galactic Plane Imaging Survey or MAGPIS (a moniker appropriate for the authors whose careers have been based on collecting random shiny objects gathered from overflights of much of the celestial sphere in several regions of the electromagnetic spectrum) is designed to provide a definitive archive of the Galactic sky at 20 cm.

In Section 2 we describe the survey parameters and the data acquired to date; in addition, we discuss complementary datasets we have used in our analysis and introduce the MAGPIS website, which offers comprehensive access to all of our data products. Section 3 outlines our analysis strategy, presents the imaging results, and provides a statistical characterization of the survey sensitivity threshold and dynamic range. We then discuss our detection algorithms for both discrete and diffuse sources, and present the source catalogs as well as an atlas for all extended emission regions (§4). Section 5 includes a discussion of a preliminary comparison between MAGPIS and the MSX mid-IR data, and previews the prospects for a more complete census of H II regions in the first quadrant. This is followed by a discussion (§6) of the nonthermal emission regions detected in our survey, including the discovery of several dozen new supernova remnant candidates. We summarize our results in Section 7.

2. THE MAGPIS SURVEY: DESIGN AND DATA ACQUISITION

As noted above, radio emission is a prominent signature of massive stars; H II regions, pulsars, supernova remnants, and black hole binaries are all the products of O and early B stars that have a small scale height. This fact, coupled with constraints on the total observing time available, has led us to restrict our Galactic latitude coverage to $|b| < 0.8^\circ$. This is greater than the OB star scale height (Reed 2000) for all distances beyond 3 kpc and covers a region up to $z = \pm 230$ pc at the solar circle on the far side of the Galaxy (we adopt $R_\odot = 8.5$ kpc throughout).

2.1. The 20 cm data

Our first tranche of Galactic longitude, $32^\circ > l > 19^\circ$, was chosen to complement our first X-ray data set and to explore the tangent to the Scutum spiral arm. The second segment we have completed covers the region $19^\circ > l > 5^\circ$; we stopped at 5° mainly because the central regions have been reasonably well-mapped previously. We intend to continue the survey as time becomes available, first to the GLIMPSE upper longitude limit of $l = 65^\circ$ and later to both higher and lower longitudes.

Data are collected in the B-, C-, and D-configurations of the

TABLE 1
OBSERVING LOG

Description	B	VLA Configuration		
		C	D	BnC
Phase 1, 20 cm ^a	Mar–Apr 2001 31 hrs	Aug–Sept 2001 28 hrs	Aug–Sept 2000 28 hrs	May 2001 1.5 hrs
Phase 2, 20 cm ^b	Jan 2004 36 hrs	Feb–Mar 2004 19 hrs	Apr 2003 18 hrs	
Phase 1, 90 cm ^c		Sept 2001 3.5 hrs		

^a20 cm Phase 1: $19^\circ < l < 32^\circ$, $|b| < 0.8^\circ$

^b20 cm Phase 2: $5^\circ < l < 19^\circ$, $|b| < 0.8^\circ$

^c90 cm Phase 1: $20^\circ < l < 33^\circ$, $|b| < 2^\circ$

VLA operating in pseudo-continuum mode at 20 cm; two 25-MHz bandwidths centered at 1365 MHz and 1435 MHz are broken into seven 3 MHz channels to minimize bandwidth smearing as well as to reduce significantly our sensitivity to interference. The loss of a factor of two in bandwidth over the standard continuum mode is not important, since virtually all maps are dynamic-range, rather than sensitivity, limited.

The pointing pattern is displayed in Figure 1. The close-packed hexagonal array provides uniform coverage with a peak-to-minimum variation in sensitivity of $< 20\%$ (after co-adding of adjacent images — see Fig. 2). We observe each location four times in each of the three configurations spaced roughly equally in hour angle over a range ± 4 hrs to maximize uv coverage; the result is an average of ~ 12 minutes per field per configuration, providing a theoretical noise level (~ 0.08 mJy) far below the dynamic range limit of the maps. In the second round of observations we have saved observing time by using the full 12 minutes per field in the B configuration, but reducing the integration time by a factor of two in the two lower-resolution configurations (while maintaining the observational cadence at multiple hour angles). This reduces our sensitivity by $\sim 20\%$ in the least-populated map regions, although, again, most of the images are dynamic-range limited and the effect on the final source catalog is minimal.

A total of 165 hours of time has been accumulated to date in the MAGPIS project. Table 1 lists the observing epochs and configurations used to construct the 252 individual images, which cover an area of over 42 deg^2 .

2.2. The 90 cm data

Even with high-quality images, a single frequency is insufficient to identify source classes unambiguously and to disentangle thermal and nonthermal emission in crowded regions. As part of our initial observation program for MAGPIS, we obtained 3.5 hours of 90 cm pseudo-continuum observations in the C configuration of the VLA during September of 2001. Eight pointings were used to cover the region $20^\circ < l < 33^\circ$, $|b| < 2^\circ$. The data were reduced using a $15''$ pixel size and have a resolution of $\sim 70''$. In addition, we retrieved from the VLA archive 90 cm data originally taken by Brogan et al. (2005) that cover the remainder of our current survey area ($3.6^\circ < l < 20^\circ$, $|b| < 2^\circ$). These data were reduced using a $6''$ pixel size and have a resolution of $\sim 25''$.

2.3. The mid-IR data

We have retrieved the mid-IR images and catalogs of the Midcourse Space Experiment (MSX – Price et al. 2001)

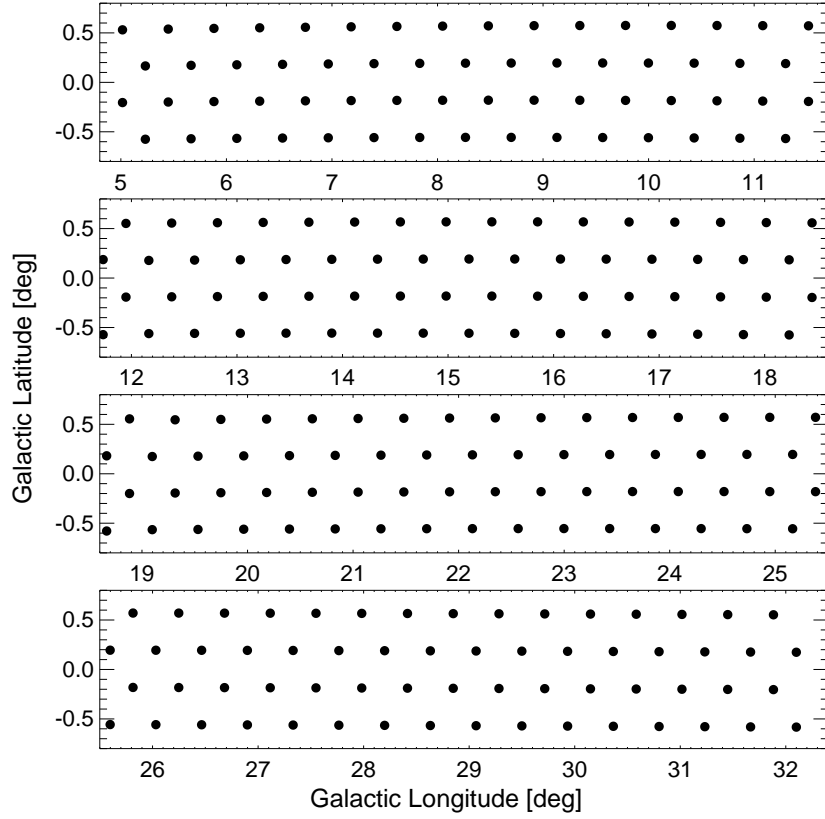


FIG. 1.— The hexagonal grid of 252 VLA pointing centers used for the MAGPIS 20 cm survey.

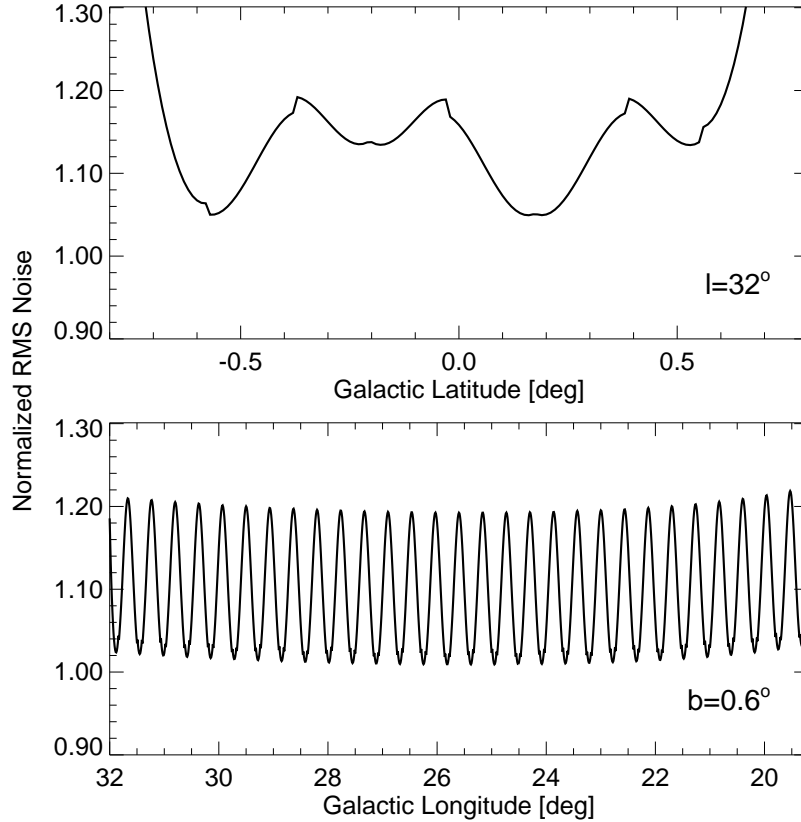


FIG. 2.— The variation in the rms noise as a function of position after the overlapping images have been co-added. The rms is normalized to unity at field center for a single pointing. The top panel shows a cut in latitude at the edge of the survey ($l = 32^\circ$), and the bottom panel shows the rms along a line passing near the field centers at $b = 0.6^\circ$. The rms noise is uniform, with a peak-to-peak variation of only $\sim \pm 10\%$ except at the edges of the surveyed area.

from the IPAC database for the regions our survey covers to date. For ease of comparison, we have regridded the E-band ($20\mu\text{m}$) data onto the same l, b grid used to present the primary MAGPIS images. We have also constructed ratio maps for the 20 cm and $20\mu\text{m}$ data for use in separating thermal and nonthermal emission. An example of such an image is displayed in Figure 3. High values of the radio-to-IR ratio generally indicate nonthermal radio emission such as is produced by supernova remnants, while low values tend to highlight dusty H II regions, although pulsar wind nebulae, dusty old supernova remnant shells, and dust-free H II regions can in principle exhibit intermediate ratios. We defer a quantitative discussion of the comparison of the radio and mid-IR emission to a future paper.

2.4. The MAGPIS website

Consistent with our past practice, the raw VLA data on which MAGPIS is based have been available in the VLA archive from the day they were taken. To facilitate use of these data by the broadest possible community, we have constructed the MAGPIS website (<http://third.ucllnl.org/gps>), which presents our data products in easily accessible forms. In addition to the full-resolution 20 cm images, the site provides the complementary 90 cm images, the regridded MSX $20\mu\text{m}$ images, and an image atlas of diffuse emission regions (see below). The single-configuration 6 and 20 cm images from our earlier snapshot surveys (White, Becker & Helfand 2005) are also available. Images can be displayed with user-specified coordinates, box sizes, and intensity scales or can be downloaded as FITS files. The full discrete-source and diffuse catalogs are available for retrieval or through a search query function, as are our catalogs and publications from our earlier snapshot survey work. We expect to add our XMM X-ray survey data and the Spitzer GLIMPSE survey images and catalogs as they become available.

3. THE MAGPIS IMAGES

In contrast to the extragalactic radio sky, which is rather sparsely populated by mostly compact sources, radio emission in the Galactic plane is dominated by bright, diffuse H II regions and supernova remnants. Thus, the single-snapshot observations and two-dimensional mapping approximations that worked well in the FIRST and NVSS surveys are inadequate for producing high-dynamic-range images for MAGPIS. In this case, the VLA data must be treated as a three-dimensional data set. In practice, 3-d distortions scale with offset from the image center; thus, one way to minimize 3-d effects is to tile the VLA's $30'$ primary beam with many small images. We have used a grid of 21 by 21 images, each of which is 128 by 128 pixels in size. Our initial data were reduced on a Sun Ultra 60, with each image requiring ~ 12 hours to CLEAN. We subsequently migrated the analysis to a dual-processor Pentium 4 computer that is approximately seven times faster. Since the images are greatly improved by self-calibration, each field has to be reprocessed several times.

Even with data from the D configuration, the resulting maps suffer missing flux from large-scale structure ($\gg 1'$) to which the VLA is insensitive. To correct for this deficiency, we combined the VLA images with images from a 1400 MHz survey made with the Effelsberg 100-m telescope ($\sim 7'$ angular resolution). The AIPS task IMERG makes FFTs of both the VLA and Effelsberg images, combines the derived FFT amplitudes, and then converts back to the image plane to produce the fi-

nal individual images. We use a $6''.2 \times 5''.4$ restoring beam on maps with a pixel size of $2''$. The individual maps are ultimately summed and rebinned to produce mosaic images in Galactic coordinates. The dynamic range varies somewhat with location but, measured as a ratio of the peak flux in the brightest source to the full image rms, is typically in excess of 1000:1 in a 1 deg^2 image. Over most of the images, 1 mJy point sources are easily detected.

4. THE MAGPIS CATALOGS

The large, diffuse emission features and variable background, coupled with source size scales ranging from arcseconds to degrees, render impractical the type of automated source detection algorithms applied to extragalactic radio surveys. Thus, we have employed the human eye-brain detection system to search the 16.7 million MAGPIS beam areas for radio sources. We divided the problem into two parts: the detection and cataloging of discrete objects less than a few beam areas in size and unconfused by extensive diffuse emission, and regions of sky in which significant diffuse emission is present.

4.1. Discrete source detection

A square field was defined around each candidate discrete source. In cases where it was impossible to isolate a single emission peak (e.g., for overlapping or closely clustered sources), multiple sources were included in one field and the field was flagged as "multiple". The default field size was $34'' \times 34''$, but this size was adjusted for larger sources (increased), for high density areas (decreased), or for other reasons (increased or decreased on a case by case basis) such as nearby bad pixels, proximity to the edge of the maps, etc. For the entire survey area this process yielded 2628 single-source fields, and 467 multiple-source fields.

The AIPS task HAPPY (see White et al. 1997) was then run on each of the fields. In HAPPY, a local rms level was calculated for each field using an area of three times the input field area; a minimum detection level of five times the local rms was set for each field.

Using the HAPPY output, we rejected any source with a fitted peak flux, $F_p < 1.0\text{ mJy}$ or ≤ 5.0 times the local rms, whichever is higher. We also rejected any source with a fitted minor axis less than $3''.5$ (the beam minor axis is $5''.2$, and experience from the use of HAPPY in the FIRST survey shows that the vast majority of such "skinny" sources are spurious sidelobes); this only eliminated one source that passed the F_p and rms criteria. This process yielded a catalog of 3229 sources.

Although restricting HAPPY to predetermined fields around candidate sources should reduce the number of spurious detections, this method is still susceptible to poor fits resulting from complex, extended emission as well as areas of patterned noise near bright sources. To assess these potential causes of contamination, we flagged for further examination HAPPY solutions

1. when HAPPY fit more than one source in a single-source input field (67 fields, 144 sources);
2. when HAPPY fit more than two sources in a multiple-source input field (69 fields, 219 sources); or
3. when any fit not meeting (1) or (2) had a major axis $> 15''$, a major to minor axis ratio greater than 2.0, or $F_{\text{int}}/F_p > 5.0$ (136 fields, 143 sources).

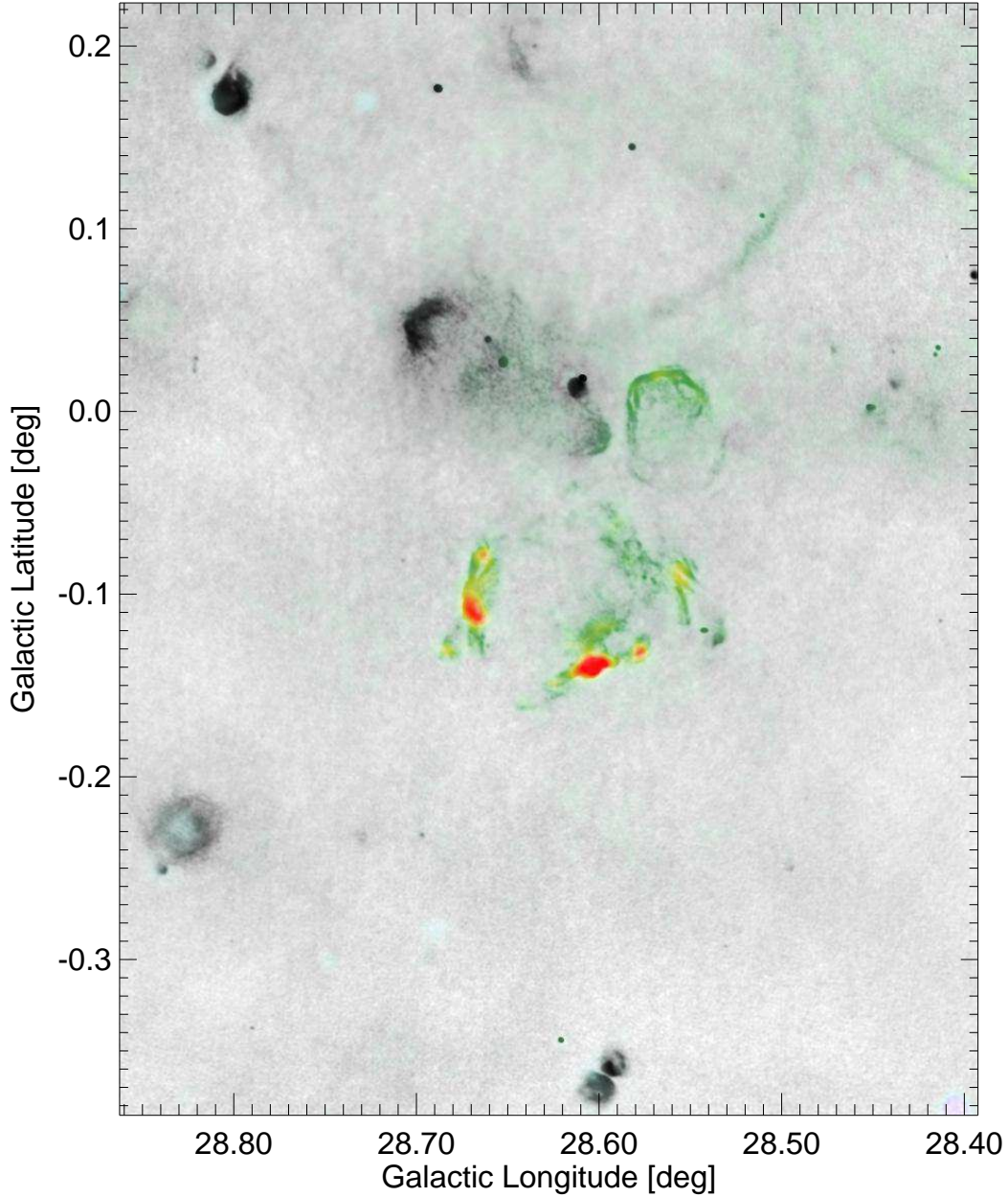


FIG. 3.— Combined radio-IR image demonstrating the separation of thermal and non-thermal emission. The radio image is used to set the intensity of the displayed image, while the radio-IR flux ratio is used to set the color hue and saturation. Objects with strong IR emission (typical of thermal radio sources) appear in black and white, while objects that have absent or weak IR emission (typical of nonthermal radio sources) appear in colors ranging from green to red depending on the upper limit on the radio-to-IR ratio. Both the known SNR G28.6-0.1 and a previously undiscovered remnant at G28.56-0.01 are apparent, as are a half-dozen thermal sources with varying morphologies.

In total, 506 fields were flagged and examined. Of these 338 were determined to be good fits, 88 to be “acceptable” fits, 56 to be artifacts or noise, and 24 to be extended rather than discrete sources; the latter were moved to the extended source atlas (see below) and the artifacts were deleted.

The 88 “acceptable” fits are all (in our best judgement) real radio sources, but they are distinguished from good fits in that, upon inspection, it is clear that the two-dimensional Gaussian employed by HAPPY is a poor representation of the source surface brightness distribution. We report their HAPPY-derived parameters in Table 2 for consistency, but flag them accordingly.

The final catalog, presented in Table 2, includes 3149 dis-

crete sources. A Galactic longitude \pm latitude-based name (col. 1) is followed by the peak and integrated flux densities from the Gaussian fit (cols. 2 and 3), with the S_i value flagged for the “acceptable” fits described above, and the estimated rms noise level (col. 4). The major and minor axes (full-width at half-maximum) and position angle for the elliptical Gaussian complete the morphological description of these compact sources. The last two columns give the infrared $8\ \mu\text{m}$ and $21\ \mu\text{m}$ flux densities for sources with MSX matches (described further below in §5.1).

Owing to the variable background and numerous regions of bright diffuse emission, the threshold for discrete source detection varies significantly over the survey region. We can

obtain a mean value for the threshold by comparing the source surface density with that of the FIRST survey. That survey covers 9033 deg^2 of the extragalactic sky and includes 781,450 sources not flagged as sidelobes, for a mean surface density of 86.54 deg^{-2} at a flux density threshold of 1.0 mJy ⁶. The mean source surface density of discrete sources in MAGPIS is 74.8 deg^{-2} considering the entire survey area of 42.1 deg^2 and 73.0 deg^{-2} in the 35.6 deg^2 lying outside regions of diffuse emission; the former value is higher owing to source clustering. Matching this surface density while allowing for several hundred true Galactic sources outside regions of diffuse emission (see §5.1), we find an effective discrete source threshold of $\sim 1.5 \text{ mJy}$ that yields 58.6 extragalactic sources deg^{-2} in *FIRST*. Thus, our survey is significantly incomplete between the minimum reported flux density of 1 mJy and $\sim 2 \text{ mJy}$, but, over the 85% of the area outside regions of diffuse emission, it is largely complete above this range. Note that a large majority of the discrete radio sources detected even within 1° of the Galactic plane are extragalactic objects; this is evident from the lack of a strong Galactic latitude dependence of our source counts seen in Figure 4. Observations at other wavelengths are required to identify the Galactic components of the discrete source population.

4.2. The diffuse source atlas

The elliptical Gaussians used in fitting the discrete sources are a poor approximation to the surface brightness distributions for nearly all of the more extended radio sources detected in our survey. Furthermore, for sources extended by more than $\sim 60''$, our VLA uv coverage is inadequate to derive accurate flux densities, and the addition of the single dish data, while an asset in making images, has unquantifiable effects on derived flux densities. Thus, we again turn to the eye-brain system for identifying diffuse sources and source complexes, and do not attempt to derive accurate flux density measurements for these sources.

The entire survey region was examined by eye, and regions of extended emission were identified and enclosed in square boxes ranging in size from 1 arcmin^2 to $48' \times 48'$. In some instances regions are defined by a single coherent source, while in others a complex of diffuse emission regions is included. A total of 398 such regions covering 7.6 deg^2 were so identified. For each region, the peak flux density, minimum flux density (a proxy for the noise level in the region), total area, and net flux density were recorded; we emphasize that these flux densities are not necessarily accurate reflections of integrated source intensity and, in some regions, include the flux density of several related – or possibly unrelated – sources; they provide only a rough guide to source intensities. We have subtracted from the integrated flux density in each region the sum of the flux densities of the discrete sources from Table 2 that fall within the region; a table listing the cataloged discrete sources within each region is available at the MAGPIS website.

In order to estimate the accuracy of our diffuse flux density estimates, we have compared our flux densities for the 25

known supernova remnants in our survey region with those tabulated in Green (2004). We exclude remnants for which the tabulated value is uncertain (listed with a “?” in Green’s catalog), as well as those that do not fall completely within our survey coverage. We scale the 1.0 GHz flux densities listed in Green’s catalog to our observing frequency of 1.4 GHz using the tabulated spectral indices. We find a good correlation between the flux densities, albeit with an offset that depends on the size of the remnant (Fig. 5). We conclude that the integrated flux densities listed for the diffuse sources typically overestimate the true fluxes of very large sources by factors of two or more due to backgrounds and confusing sources and recommend caution when using them.

The diffuse regions are cataloged in Table 3. A Galactic longitude \pm latitude-based name is found in column 1. The box size in column 2 and an intensity scaling factor for display purposes (col. 3) precede the brightest pixel value (col. 4) and its location (cols. 5 & 6), the minimum flux density recorded in the box (col. 7), and the integrated flux density inside the box (col. 8). Column 9 provides names for known supernova remnants.

Cleaving to the maxim that quantifies the relative information content of words and pictures, we have constructed a diffuse source atlas to accompany the full survey images on the MAGPIS website. Here, Table 3 is reproduced with active links that allow the user to overlay circles representing sources from the discrete source catalog and contours of the $20 \mu\text{m}$ images from the MSX catalog (Eagen et al. 2003). Each image can also be downloaded as a FITS file.

The website also includes large area ($4.5^\circ \times 1.6^\circ$) JPEG versions of the MAGPIS images with the diffuse region boxes overplotted. It is difficult to display these high-dynamic-range images with a single contrast stretch, and indeed the discrete sources are almost invisible in these images, but they are nonetheless useful for viewing the environment of the diffuse sources.

The MAGPIS discrete source catalog and diffuse source atlas provide an improvement of more than an order of magnitude in both angular resolution and sensitivity over existing Galactic plane survey data. When combined with existing catalogs at other wavelengths along with data from X-ray and infrared surveys currently underway, MAGPIS will provide a resource for studying both thermal and nonthermal processes that mark the evolution of massive stars in the Milky Way. We have a number of followup projects underway; below we briefly comment on the impact the survey is likely to have on our knowledge of the H II region and supernova remnant populations of the Galaxy.

5. GALACTIC THERMAL EMISSION REGIONS: MAGPIS AND MID-IR IMAGES

The critical dependence of an H II region’s radio luminosity on the ionizing flux of its exciting star(s) allow for the construction of a particularly pure census of massive star formation: the 20cm radio flux density falls by a factor of 300 between exciting star types O9.5 and B1 such that, at 20 kpc , O-star H II regions fall a factor of > 30 above our survey threshold, while less-massive star-forming complexes (which produce at most B stars) fall a factor > 10 below it⁷. To separate

⁶ The snapshot images of the FIRST survey require the addition of a ‘CLEAN bias’ of 0.25 mJy to the measured flux densities. The greater uv coverage achieved in the multi-array, multi-snapshot MAGPIS survey should significantly reduce CLEAN bias, although it is improbable that the bias is zero. Since, however, absolute calibration is unlikely to be accurate to better than 10% in light of our addition of single-dish data, and none of our scientific projects require flux densities this accurate, we ignore CLEAN bias in this work.

⁷ These numbers are for optically thin nebulae. Optically thick H II regions are self-absorbed at 20 cm such that only stars earlier than O7 would fall above our threshold at the far side of the Galaxy. Our old 6 cm snapshot survey allows us to find these sources down to spectral type O9.5; see Giveon et al. (2005) for details.

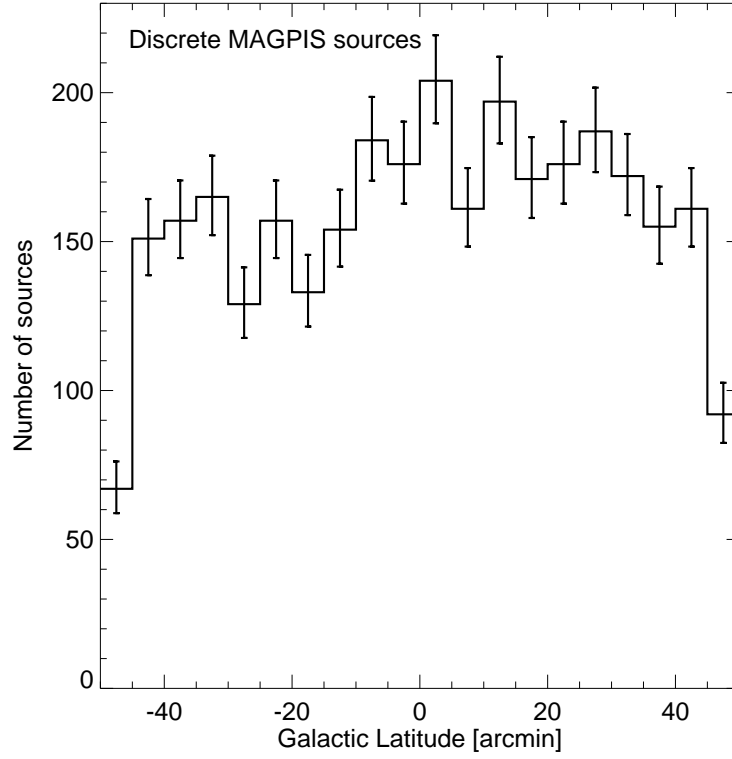


FIG. 4.— Galactic latitude distribution for the discrete source catalog. Even in the Galactic plane the 20 cm radio sky is dominated by extragalactic sources, so no strong latitude dependence is seen. The counts fall off in the $|b| > 45$ arcmin bins due to the drop in sensitivity at the edge of the survey.

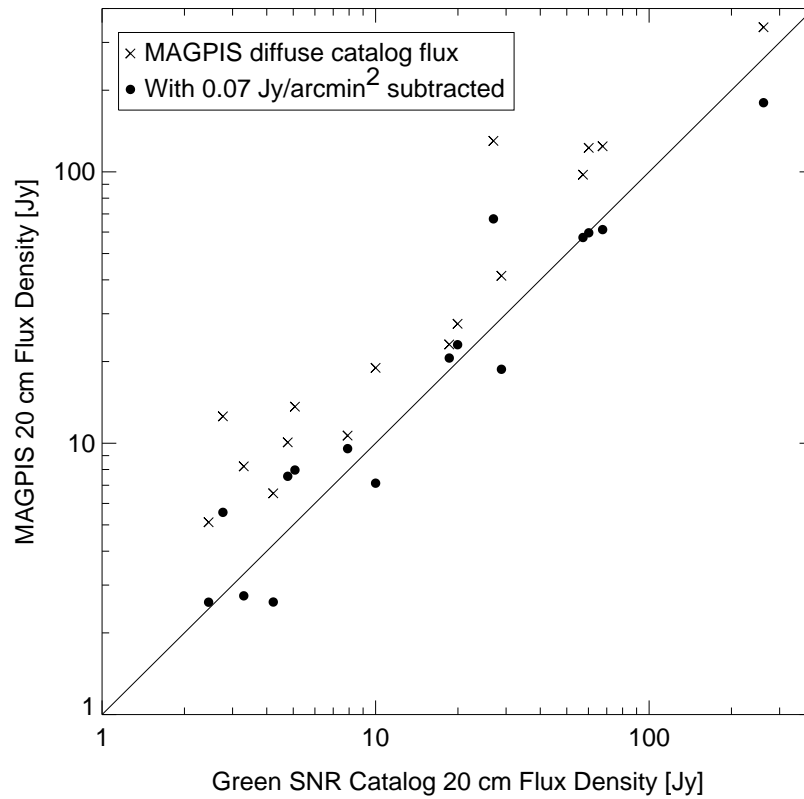


FIG. 5.— Flux densities from our diffuse source catalog for supernova remnants from the Green (2004) catalog. The x symbols show that our catalog flux densities for these extended sources are typically higher than the Green values by factors of two or more. Subtracting a corrective offset of 0.07 Jy/arcmin^2 from our flux densities improves the agreement (dots).

the H II regions from the more numerous extragalactic source populations and the extended regions of Galactic nonthermal emission requires observations at another wavelength. Our 6 cm snapshot survey is useful for the most compact sources ($D < 15''$) but resolves out flux on larger scales. Since most H II regions also contain dust that is heated by the stellar radiation, the mid-IR also can serve as a useful discriminant.

Figure 6 shows several examples of H II complexes from our radio survey with contours from the MSX $20\mu\text{m}$ images overlaid. The degree of correspondence is remarkably good and provides a straightforward method for separating thermal and nonthermal emission in star formation regions. On the MAGPIS website we also provide large-scale radio images with boxes marking the previously published H II regions collected in the Paladini et al. (2003) meta-catalog. It is clear that the MAGPIS data (along with other radio and IR surveys) will enable the construction of a vastly improved H II region catalog.

We defer a detailed analysis of the H II region population to a future paper; here we provide some simple statistics for compact and ultracompact H II regions by matching our discrete source data to the MSX catalogs as an indication of the wealth of information such a comparison contains. The higher-resolution and greater sensitivity of the Spitzer GLIMPSE data soon to become available will fill in the $2\text{--}8\mu\text{m}$ band and provide crucial information in the most crowded regions.

5.1. Match to the MSX $20\mu\text{m}$ catalog

The 20cm survey region is completely covered by the MSXPSCv2.3 "MSX6C" (Egan et al 2003) data set. We searched for MSX6C sources using a search radius of $12''$ around each of the discrete 20 cm sources. To be accepted as a match, the MSX6C source was required to have a quality flag of 2 in at least one of the four bands (see Lumsden et al. 2002). If more than one MSX6C source fell within the search radius for a single 20 cm source, the MSX6C source closest to the 20 cm source was kept (this only occurred once). A total of 376 MSX6C sources corresponding to 418 20 cm sources were matched in this manner.

To estimate the number of false matches we repeated the matching process using fake catalogs produced by shifting the MSX6C catalog $\pm 10'$ and $\pm 20'$ in longitude. Since, for example, the vast majority (78%) of the MSX sources are stars detected only in the $8\mu\text{m}$ band (very few of which have radio counterparts), we can greatly reduce the false match rate by assessing the false rates separately for sources detected in different band combinations. We have followed the methodology described in Giveon et al. (2004; see also White et al. 1991), to arrive at a false-match reliability criterion for each of the band combinations in which a 20 cm-MSX6C match existed. Using a reliability of $R > 90\%$ ⁸ we find 245 MSX6C sources (of which ~ 8 should be false) matched to 278 20 cm sources. Of these, 217 are single 20 cm-MSX6C matches, 23 are cases in which one MSX6C source matches two 20 cm sources, and 5 represent one MSX6C source matching three 20 cm sources.

The distribution of the matched and unmatched sources on the sky is displayed in Figure 7. While sources with infrared matches are found throughout the latitude coverage, it is clear

that they concentrate toward the plane. The latitude distribution is displayed in Figure 8. The distribution peaks at $b = 0^\circ$ with a surface density of $22\text{ sources deg}^{-2}$ (when regions obscured by bright diffuse sources are excluded), and has a full width half maximum of less than $15'$. Examination of the atlas of extended emission shows that there are more thermal sources inside the 6.5 deg^2 subsumed by the atlas images than outside, and most of these sources are not included in the discrete source catalog. We estimate that there are a total of more than 600 distinct H II regions in our 42 deg^2 survey area, although we defer to a future publication the development of a detailed catalog and its analysis.

6. GALACTIC NONTHERMAL EMISSION IN MAGPIS

Supernova remnants (SNRs) are among the brightest radio sources – and the brightest X-ray sources – in the Galaxy. They are a dominant source of mechanical energy input to the ISM, drive the Galaxy's chemical evolution, and mark the birthsites of neutron stars and black holes. Yet our knowledge of the Galactic population is woefully incomplete, owing to the low angular resolution of previous radio and hard X-ray surveys of the plane, and the soft spectral response of previous X-ray imaging observations. A total of 231 remnants appears in the latest catalog (Green 2004); Brogan et al. (2004) have recently added three new remnants in one of our fields. The current rate of discovery is a few remnants per year. However, based on 1) extragalactic SN rates ($\sim 1\text{--}2$ per century) combined with SNR lifetimes ($2.5\text{--}5 \times 10^4$ yr), and 2) a detailed analysis of the current SNR distribution (Helfand et al. 1989), we expect the total population to be between 500 and 1000. The youngest remnant we know is 340 years old; four to seven younger ones exist somewhere in the Galaxy.

MAGPIS can detect pulsar-driven remnants to a luminosity 10^{-4} that of the Crab Nebula at the edge of the Galaxy (or $\sim 10\%$ that of 3C58, the least luminous young Crab-like remnant known). For shell-like SNRs, our survey will be sensitive to all young remnants. For example, we will detect remnants throughout the surveyed volume down to luminosities 0.01% that of Cas A, and can even see a clone of the underluminous historical remnant SN 1006 at 20 kpc: it would appear as a $1'$ -diameter source with a flux density of $\sim 25\text{ mJy}$. Our survey could detect a remnant equivalent to SN87A from the time it was 3 years old anywhere in the survey region, and would resolve such a remnant only 15 years after the explosion.

Twenty-five known remnants fall within the current survey area, and all are easily detected. The known remnants are indicated in Table 3; in many instances, the maps presented here are the best available. Images for the eleven remnants smaller than $10'$ in diameter — most of which lack high-resolution maps in the literature — are displayed in Figure 9.

As can be seen by browsing the diffuse-source atlas, there are a large number of shell-like sources detected in our survey. Without observations at other wavelengths, however, it is impossible to separate the thermal and non-thermal sources to derive a list of new SNR candidates. Fortunately, as noted above, we do have VLA data covering the entire region at 90 cm, as well as the MSX mid-IR images. A simple qualitative comparison of these three datasets (available for the reader at the MAGPIS website) allows us to identify quickly high-probability SNR candidates.

In Table 4, we present 49 new SNR candidates in our 27° slice of Galactic longitude. To derive this list, we have required:

⁸ This eliminates MSX sources detected only in the $8\mu\text{m}$ band as well as those detected in $8\mu\text{m}$ and $12\mu\text{m}$ only, and $8\mu\text{m}$, $12\mu\text{m}$, and $14\mu\text{m}$ only. This removes 131 sources (67% of which are false matches), leading to a catalog of matches that is $> 95\%$ reliable and $\sim 90\%$ complete.

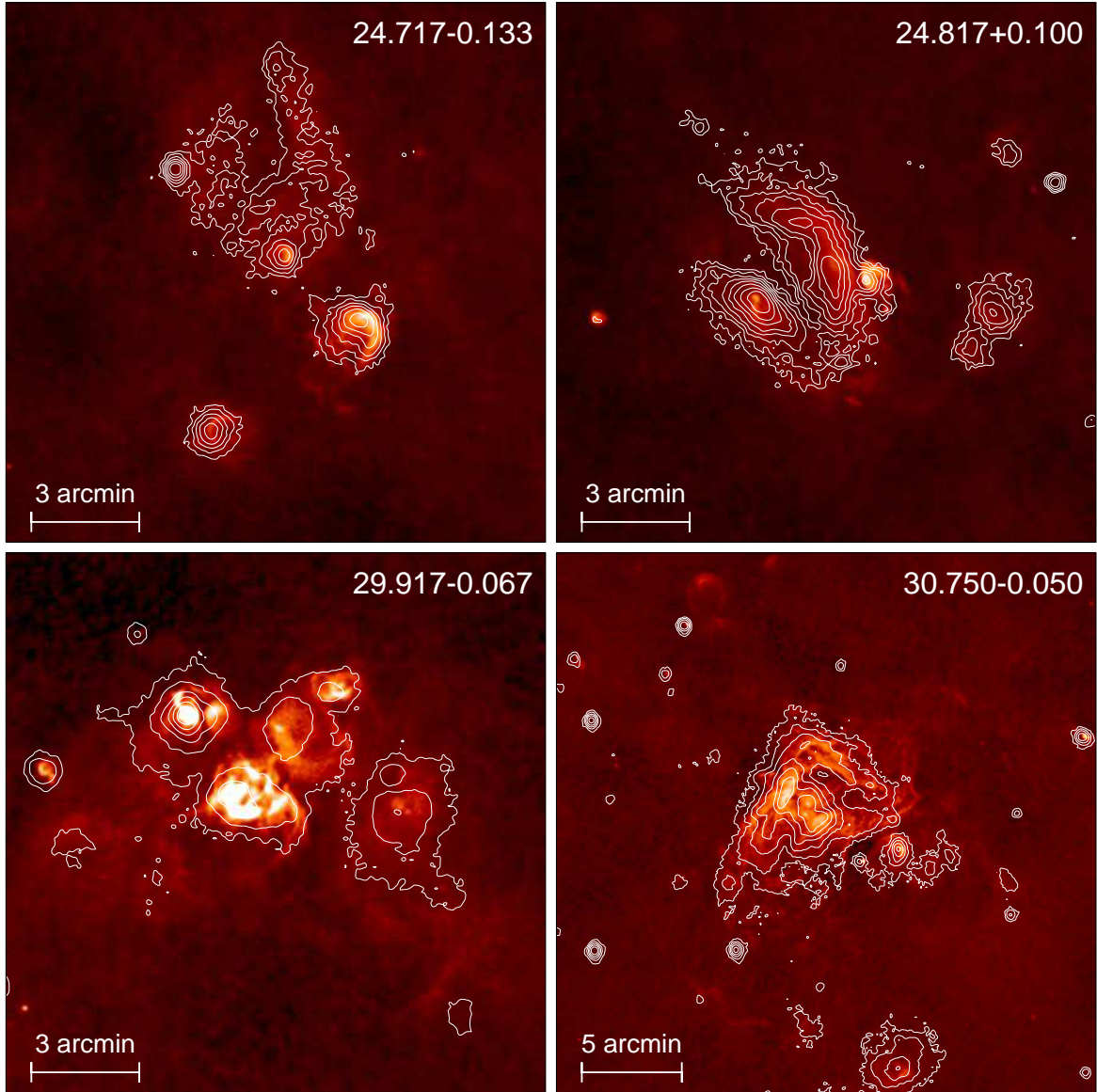


FIG. 6.— Examples of H II complexes from our radio survey with the MSX $20\,\mu\text{m}$ image contours overlaid, showing the excellent radio-IR correspondence for these thermal sources.

- the object has a very high ratio of 20 cm to $20\,\mu\text{m}$ flux (i.e., it is typically undetectable in the $20\,\mu\text{m}$ MSX image);
- the object has a counterpart in our 90 cm images with a similar morphology and a higher peak flux density; and
- the object has a distinctive SNR morphology. For shell-type remnants we require at least half of a complete shell, while for the two pulsar wind nebula candidates we see a centrally peaked brightness distribution.

For most of these candidates the data in columns 1, 3, 4 and 5 are repeated from Table 3. Column 2 gives the source diameter (as opposed to the display box size in column 3, which is always larger). Five of the entries in this table are components of larger sources listed in Table 3, with three associated with the large diffuse complex at G19.60–0.20 and two associated with G6.50–0.48.

Images for a dozen candidates ranging in size from $40''$ to $9'$ are displayed in Figure 10. Not unexpectedly, the diameter distribution for our remnant candidates varies markedly from that of the known remnant population. Assuming that followup spectral and polarimetric observations confirm the large majority of these sources as SNRs, we will have tripled the number of known remnants in this region of the Galaxy. However, while the number of remnants with $D \geq 10'$ will only rise from 13 to 16, the number with $10' > D \geq 5'$ will quadruple from 5 to 19, while the number with $D < 5'$ will rise more than sevenfold from 5 to 37.

Particularly interesting among these new SNR candidates are those that may harbor young, high- \dot{E} pulsars. In addition to the two PWN candidates, there are two shell-like remnants with central diffuse emission peaks highly reminiscent of composite SNRs. Given the core-collapse SN rate in the Galaxy, we should expect to find ~ 10 neutron stars younger than the Crab and 3C58 pulsars. While these new sources are significantly dimmer than even the underluminous PWN

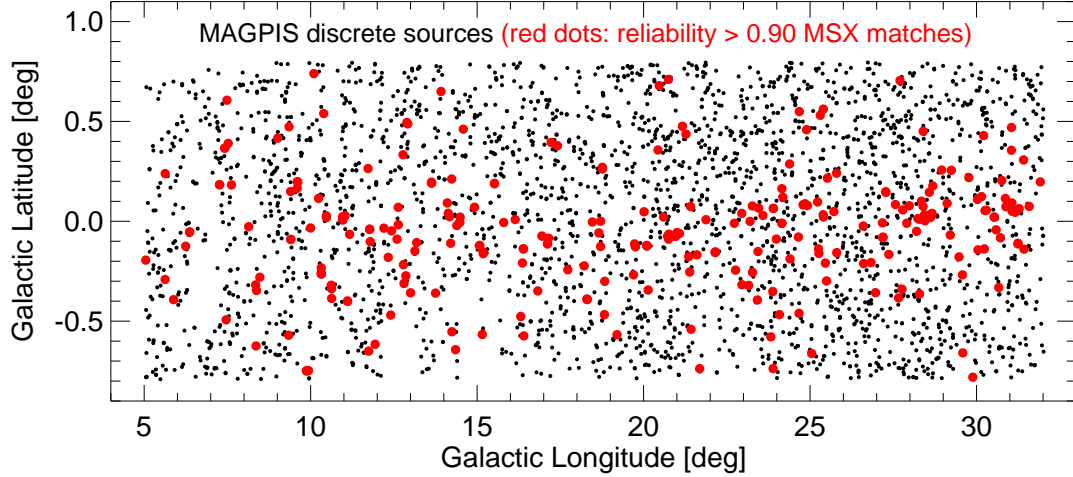


FIG. 7.— Sky distribution of MAGPIS 20 cm radio sources from the discrete source catalog. Red dots show sources with confident (reliability > 0.90) infrared counterparts in the MSX catalog. The radio-MSX matches are clearly concentrated toward the plane.

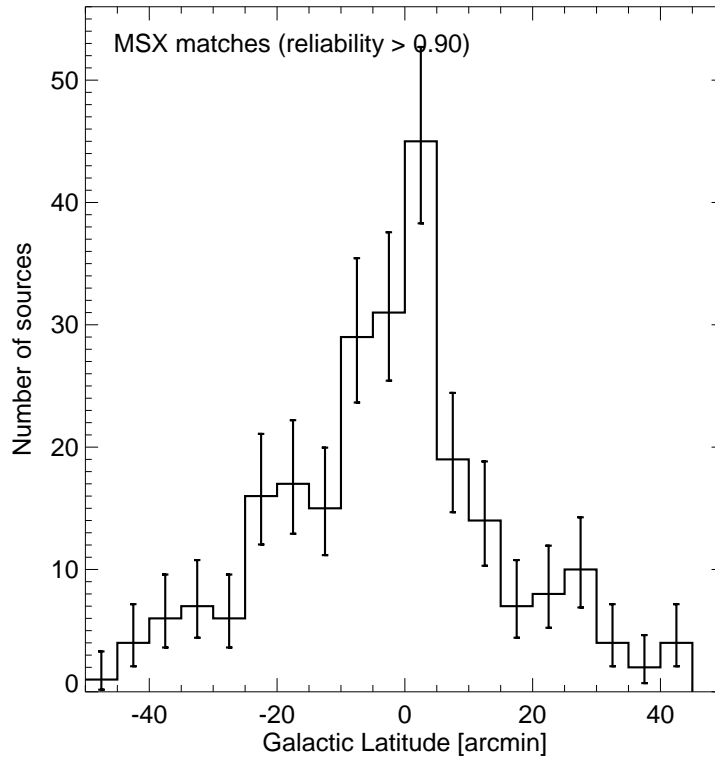


FIG. 8.— Galactic latitude distribution for the 245 MSX sources having reliable radio matches. These sources are highly concentrated toward the plane of the Galactic disk.

3C58, if they are at distances of ~ 15 kpc, their luminosities are comparable. Also noteworthy are the three shell-type remnants with diameters less than $1'$. At 15 kpc, their diameters are ~ 3 pc, corresponding to an age of ~ 130 years for a radio expansion rate comparable to that of SN87A.

The SNR candidates listed in Table 4 far from exhaust the nonthermal emission features in our survey area; a roughly comparable number of filaments and arcs with apparently nonthermal radio spectra and no IR counterparts are seen.

Furthermore, there are several regions in which thermal and nonthermal features are cospatial; these will require scaled-array observations at several frequencies to disentangle. Nonetheless, it is clear that high-dynamic-range, high-sensitivity observations of the type reported here are essential for characterizing fully the Galactic SNR population.

7. SUMMARY AND FUTURE PROSPECTS

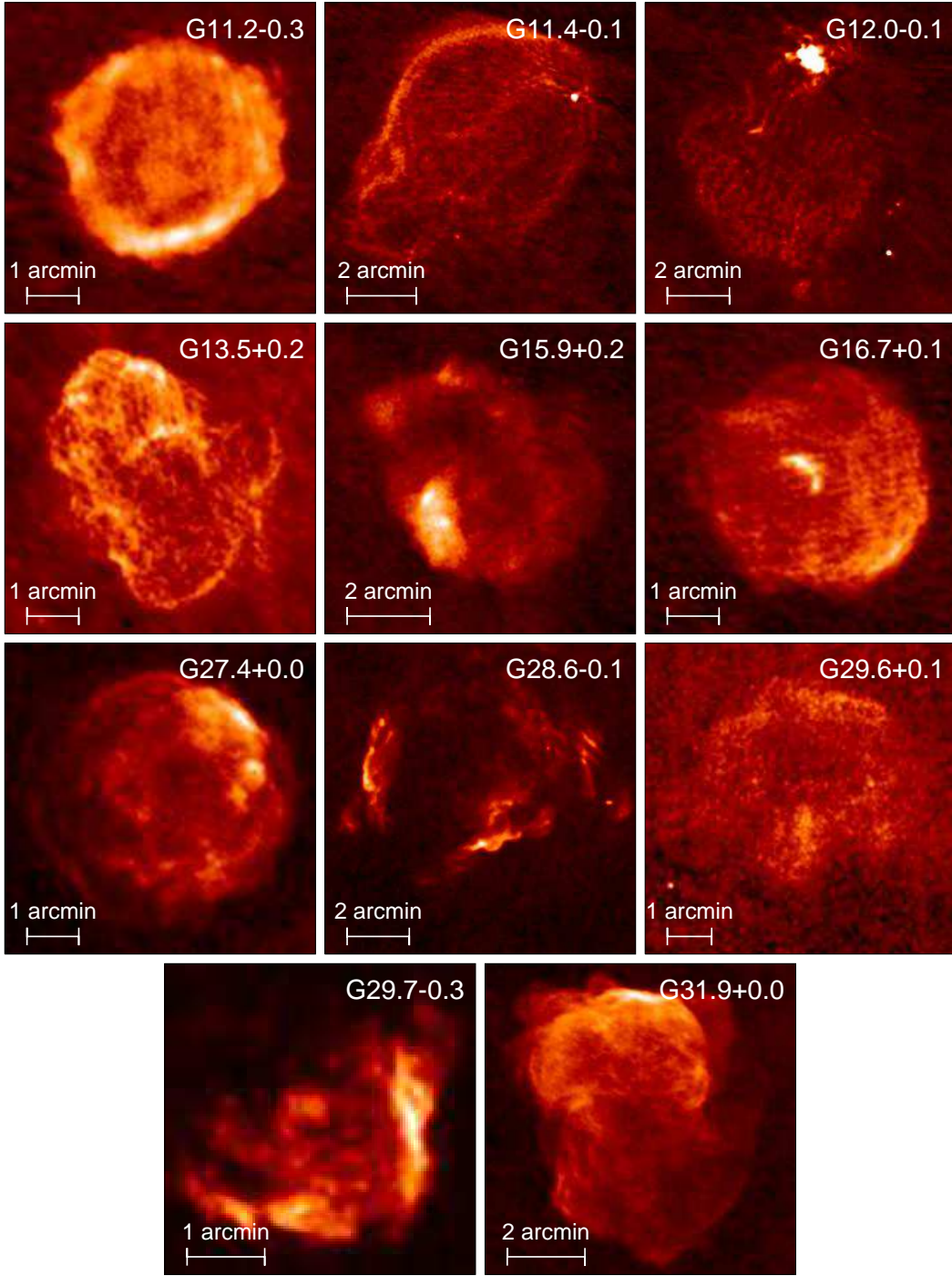


FIG. 9.— MAGPIS 20 cm images of the eleven known supernova remnants in the survey area with diameters less than $10'$.

We have presented a centimetric image of the plane of the Milky Way in the first quadrant that represents an improvement over existing surveys by more than an order of magnitude in resolution, sensitivity, and dynamic range. The survey detection threshold is 1 to 2 mJy over most of the survey area. We identify over 3000 discrete radio sources and ~ 400 regions of diffuse emission, presenting catalogs and atlases that quantify the source properties. We include complementary 90 cm images over the entire survey region and provide a comparison with mid-IR data; taken together, these latter two datasets help to separate thermal from nonthermal emission

regions. We find several hundred H II regions in the survey area, many reported here for the first time. We also identify 49 high-probability supernova remnant candidates, including a seven-fold increase in the number of remnants with diameters smaller than $5'$ in the survey region. All of the survey's results are available at the MAGPIS website.

Considerable work remains to exploit fully the survey results. A complementary hard X-ray survey over portions of this region is being conducted with XMM-Newton, and several followup observations of interesting sources are scheduled with XMM and Chandra. Scaled-array polarimetric and pho-

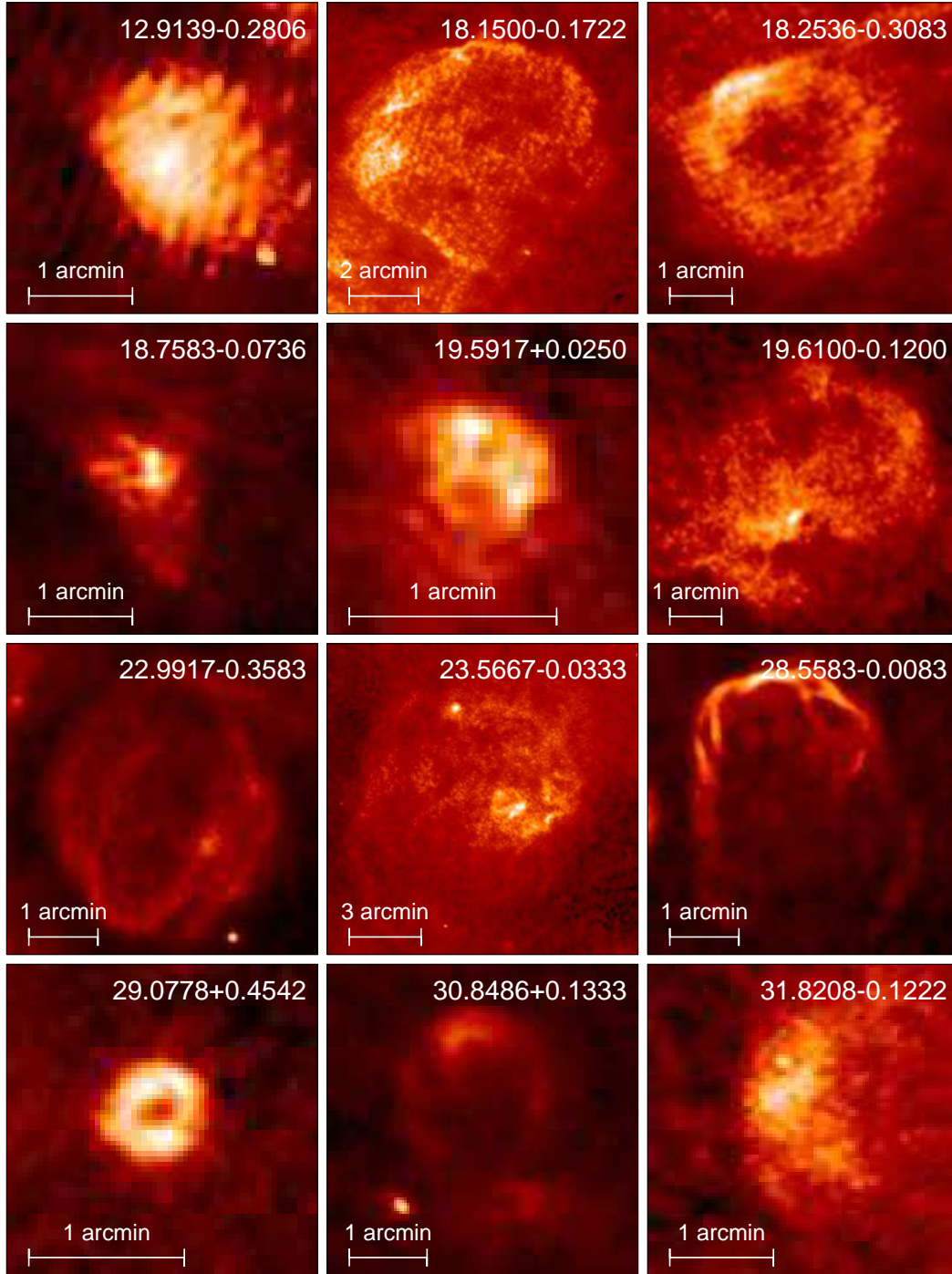


FIG. 10.— MAGPIS 20 cm images of 12 new supernova remnant candidates.

tometric observations with the VLA are required to confirm the SNR candidates. As the Spitzer GLIMPSE program images become available, further progress will be possible in identifying compact and ultra-compact H II regions and in using these to provide a census of the OB star population; higher frequency observations with the VLA will be required to identify optically thick H II regions. Future observations to extend the MAGPIS coverage area will provide the basis for a comprehensive view of massive star birth and death in the Milky Way.

DJH and RHB acknowledge the support of the National Science Foundation under grants AST-05-07598 and AST-02-6-55; DJH was also supported in this work by NASA grant NAG5-13062. RHB's work was supported in part under the auspices of the US Department of Energy by Lawrence Livermore National Laboratory under contract W-7405-ENG-48. RLW acknowledges the support of the Space Telescope Science Institute, which is operated by the Association of Universities for Research in Astronomy under NASA contract NAS5-26555.

REFERENCES

Becker, R. H., White, R. L., McLean, B. J., Helfand, D. J. & Zoonematkermani, S. 1990, *ApJ*358, 485

Becker, R. H., White, R. L., Helfand, D. J. & Zoonematkermani, S. 1994, *ApJS*91, 347

- Becker, R. H., White, R. L., & Helfand, D. J. 1995, *ApJ* 450, 559
- Benjamin, R. A., et al. 2003, *PASP*, 115, 953
- Brogan, C. L., Devine, K. E., Lazio, T. J., Kassim, N. E., Tam, C. R., Briske, W. F., Dyer, K. K., & Roberts, M. S. E. 2004, *AJ*, 127, 355
- Brogan, C. L., Gaensler, B. M., Gelfand, Y., Roberts, M. E. E., Lazio, T. J., & Kassim, N. E. 2005, *X-Ray and Radio Connections* (eds. L.O. Sjouwerman and K.K Dyer) Published electronically by NRAO, <http://www.aoc.nrao.edu/events/xraydio>
- Egan, M. P., et al. 2003, *VizieR Online Data Catalog*, 5114, 0
- English, J., et al. 1998, *Publications of the Astronomical Society of Australia*, 15, 56
- Giveon, U., Becker, R. H., Helfand, D. J., & White, R. L. 2005, *AJ*, 129, 348
- Green, D. A. 2004, *Bulletin of the Astronomical Society of India*, 32, 335
- Hands, A. D. P., Warwick, R. S., Watson, M. G., & Helfand, D. J. 2004, *MNRAS*, 351, 31
- Helfand, D. J., Velusamy, T., Becker, R. H., & Lockman, F. J. 1989, *ApJ*, 341, 151
- Helfand, D. J., Zoonematkermani, S., Becker, R. H. & White, R. L. 1992 *ApJS* 80, 211
- Lumsden, S. L., Hoare, M. G., Oudmaijer, R. D., & Richards, D. 2002, *MNRAS*, 336, 621
- McClure-Griffiths, N. M., Green, A. J., Dickey, J. M., Gaensler, B. M., Haynes, R. F., & Wieringa, M. H. 2001, *ApJ*, 551, 394
- Paladini, R., Burigana, C., Davies, R. D., Maino, D., Bersanelli, M., Cappellini, B., Platania, P., & Smoot, G. 2003, *A&A*, 397, 213
- Price, S. D., Egan, M. P., Carey, S. J., Mizuno, D. R., & Kuchar, T. A. 2001, *AJ*, 121, 2819
- Reed, B. C. 2000, *AJ*, 120, 314
- White, R. L., Becker, R. H. & Helfand, D. J. 1991 *ApJ* 371, 148
- White, R. L., Becker, R. H., Helfand, D. J. & Gregg, M. D. 1997, *ApJ* 475, 479
- White, R. L., Becker, R. H., & Helfand, D. J. 2005, *AJ*, 130, 586
- Zoonematkermani, S., Helfand, D. J., Becker, R. H., White, R. L. & Perley, R. A., 1990, *ApJS* 74, 181

TABLE 2
CATALOG OF DISCRETE SOURCES

Name ° (1)	$S_p(20\text{cm})^a$ mJy/beam (2)	$S_i(20\text{cm})^b$ mJy (3)	RMS mJy (4)	Major ^c " (5)	Minor ^c " (6)	θ ° (7)	$S(8\mu\text{m})^d$ Jy (8)	$S(21\mu\text{m})^d$ Jy (9)
10.74968−0.41783	1.69	7.07	0.291	15.1	9.2	54.2
10.78586−0.14376	12.86	15.14	0.224	6.7	5.9	36.7
10.80070+0.15285	5.28	6.51	0.162	6.8	6.1	18.0
10.81109+0.75435	1.92	2.49	0.293	8.5	5.1	83.2
10.82677−0.01064	3.98	26.58E	0.275	17.5	12.8	16.3	1.10	1.56
10.82960−0.01145	2.05	6.68E	0.275	15.6	7.0	48.5
10.85201−0.44069	6.61	9.99	0.222	7.3	6.9	116.2
10.86448−0.32989	2.32	3.28	0.365	7.3	6.5	60.3
10.89153+0.09971	3.67	4.39	0.278	7.2	5.6	175.7
10.89487+0.06428	4.00	4.93	0.388	6.8	6.0	1.3
10.89530+0.19694	1.62	4.32	0.180	12.6	7.1	54.2
10.89687+0.19994	4.04	6.13	0.180	7.6	6.7	31.6
10.89866+0.20285	1.19	3.28	0.180	11.3	8.2	116.6
10.91317+0.23448	30.65	51.38	0.207	8.2	6.9	137.6	0.16	< 1.34
10.91841−0.48325	1.36	2.54	0.218	9.9	6.3	9.1
10.92542+0.02681	69.34	83.74	0.308	6.6	6.2	32.0
10.93848+0.41073	2.58	2.93	0.203	6.9	5.5	41.9
10.94310−0.40329	5.73	22.67	0.258	12.4	10.6	94.2
10.94413+0.63106	4.33	5.63	0.186	6.8	6.4	2.9
10.95074+0.23027	1.78	2.28	0.236	7.1	6.0	155.7
10.95235−0.48679	1.17	2.45	0.217	9.9	7.1	77.8
10.95854+0.02233	37.32	47.92	0.395	6.8	6.3	27.7	0.35	12.58
10.96456+0.00641	24.92	196.93E	0.370	23.7	11.2	168.1	1.95	11.42
10.96557+0.00971	46.57	207.93	0.370	14.7	10.2	159.4	1.95	11.42
10.96678+0.45096	8.77	10.53	0.204	6.6	6.1	37.2
10.97994+0.47065	1.66	2.76	0.213	7.8	7.1	44.1
10.98345+0.46966	1.26	2.33	0.213	9.4	6.6	67.0
10.98584+0.70115	47.01	49.54	0.214	6.4	5.5	28.8
10.99897+0.16847	22.35	26.37	0.225	6.5	6.1	26.8
11.00796+0.58933	17.50	18.61	0.166	6.5	5.5	30.9
11.02311+0.32766	2.35	2.94	0.229	6.8	6.2	170.8
11.02444+0.25564	3.39	4.10	0.217	6.7	6.1	0.6
11.03023+0.05336	5.64	14.01	0.318	9.8	8.5	92.3
11.03291+0.02761	2.95	3.71	0.280	7.0	6.0	71.9	0.44	2.52
11.03867−0.03903	6.80	7.98	0.267	6.6	6.0	29.0
11.04064+0.61702	1.43	1.29	0.164	6.8	4.4	14.4
11.04432+0.36909	3.86	4.48	0.215	6.7	5.8	25.7
11.05374+0.47840	3.00	2.94	0.208	6.7	4.9	24.0
11.05432+0.48628	74.63	79.12	0.204	6.3	5.6	30.3
11.06609+0.12835	1.92	2.97	0.238	9.3	5.6	29.0
11.07328+0.60324	1.47	1.83	0.146	7.4	5.6	50.7
11.07971+0.12145	1.78	3.67	0.236	10.6	6.5	31.8
11.11013−0.39894	87.96	253.15	0.422	10.8	8.9	22.3	5.05	68.05
11.11020−0.40122	32.79	127.79	0.422	14.9	8.8	177.1	5.05	68.05
11.11674−0.65359	1.79	3.81	0.259	10.2	7.0	132.5
11.11810−0.65584	1.45	3.08	0.259	12.8	5.5	35.3
11.13753−0.21337	4.82	6.26	0.191	7.2	6.0	41.8
11.14507−0.14098	1.12	2.17	0.192	10.5	6.2	42.6
11.14767+0.70009	1.65	2.82	0.185	9.0	6.3	176.6
11.16342+0.77554	1.67	5.11	0.262	11.4	8.9	156.2

NOTE. — Table 2 is published in its entirety in the electronic edition of the *Astronomical Journal* and is also available on the MAGPIS website (<http://third.ucllnl.org/gps>). A portion is shown here for guidance regarding its form and content.

^a Peak flux density at 20 cm.

^b Integrated flux density at 20 cm. An appended 'E' indicates that the Gaussian model is inadequate and that the value is probably inaccurate.

^c Full-width at half-maximum for major and minor axes of the elliptical Gaussian fit. The CLEAN beam ($6''.2 \times 5''.4$) determines the size for unresolved sources.

^d The $8\mu\text{m}$ and $21\mu\text{m}$ infrared fluxes come from the MSX6C catalog (Egan et al. 2003).

TABLE 3
CATALOG OF DIFFUSE EMISSION REGIONS

Name $(l+b)$ $^{\circ}$	Box Size arcmin	Scale mJy/beam	S_p mJy/beam	l_p $^{\circ}$	b_p $^{\circ}$	S_i Jy	Comment
(1)	(2)	(3)	(4)	(5)	(6)	(7)	(8)
5.1917–0.2833	2	15	17.0	5.1903	–0.2838	1.05	
5.4444+0.2056	1	3	2.3	5.4466	+0.2052	0.136	
5.4667+0.3833	6	1	1.7	5.5155	+0.3474	1.92	
5.4750–0.2458	6	7	114.3	5.4749	–0.2432	4.04	
5.5250+0.0292	4	5	7.5	5.5228	+0.0285	1.04	
5.9000–0.4333	20	20	199.5	5.8851	–0.3924	56.9	
5.9306–0.0972	2	4	3.8	5.9301	–0.0992	0.481	
5.9500+0.0833	25	10	175.7	5.9440	+0.2013	47.9	
6.0158–0.3650	2	5	5.5	6.0146	–0.3647	0.765	
6.0806–0.1167	5	10	16.1	6.0818	–0.1181	6.07	
6.1000+0.5000	25	4	7.1	6.1624	+0.4969	17.3	
6.1075–0.1731	1	5	6.1	6.1085	–0.1720	0.289	
6.1500–0.6250	6	5	5.1	6.1346	–0.6352	5.25	
6.2000+0.1833	11	3	3.7	6.2235	+0.1897	15.2	
6.2417–0.5653	4	5	82.8	6.2085	–0.5475	1.91	
6.2653–0.6458	2	2	2.6	6.2629	–0.6475	0.516	
6.3333+0.5500	11	1	1.6	6.3191	+0.6019	1.99	
6.4167–0.1667	48	15	200.0	6.5753	+0.1897	341	SNR G6.4-0.1 (W28)
6.5000–0.4800	24	6	17.2	6.5664	–0.3025	123	
6.5528–0.0958	3	90	123.2	6.5519	–0.0975	6.16	
7.0167–0.2500	12	10	10.4	6.9814	–0.2864	26.7	
7.0417+0.1750	2	8	8.5	7.0419	+0.1786	0.58	
7.0700–0.1000	17	5	3.4	7.2042	–0.2347	18.2	SNR G7.0-0.1
7.1764+0.0875	3	5	4.8	7.1769	+0.0853	0.704	
7.2167+0.1833	10	5	17.2	7.2658	+0.1831	9.10	
7.2600–0.1400	11	6	6.1	7.2536	–0.0753	13.2	
7.4000+0.6750	10	3	3.1	7.3658	+0.6853	4.97	
7.4300+0.3500	15	1.5	16.2	7.4203	+0.3664	7.50	
7.4722+0.0583	1	150	218.3	7.4714	+0.0581	2.10	
7.7972–0.6333	4	2	2.4	7.7942	–0.6292	1.00	
8.0750–0.1083	13	4	34.0	8.1392	–0.0270	15.2	
8.1250–0.4722	12	1.5	5.0	8.1892	–0.3986	11.1	
8.1417+0.2292	7	40	229.5	8.1403	+0.2236	10.7	
8.2514–0.4403	2	2	2.1	8.2498	–0.4441	0.363	
8.3083–0.0861	6	15	263.5	8.3387	–0.0931	7.00	
8.3583–0.3000	4	10	12.4	8.3498	–0.3187	3.61	
8.3750–0.3514	2	10	17.0	8.3754	–0.3464	1.28	
8.4167–0.3472	2	5	4.5	8.4170	–0.3453	0.913	
8.4333–0.2764	2	7	7.3	8.4326	–0.2781	0.629	
8.6000–0.2500	15	3	5.2	8.5104	–0.2636	43.7	
8.6625–0.3417	3	30	192.3	8.6688	–0.3559	1.60	
8.7000–0.1000	30	7	21.0	8.5265	+0.0891	124	SNR G8.7-0.1 (W30)
8.8583–0.2583	6	3	3.4	8.8427	–0.2481	4.79	
8.8667–0.3250	3	10	12.7	8.8722	–0.3215	1.85	
9.1750+0.0333	6	3	8.2	9.1576	+0.0162	3.16	
9.6167+0.2000	3	30	98.5	9.6167	+0.1952	1.73	
9.6319+0.4833	6	2	1.6	9.6167	+0.4674	2.00	
9.6833–0.0667	12	4	7.2	9.6639	–0.0504	12.5	
9.7833+0.5667	16	3	5.1	9.7567	+0.5380	8.22	SNR G9.8+0.6
9.8750–0.7500	2	50	55.2	9.8756	–0.7491	0.633	
9.9667–0.7472	10	4	37.5	10.0501	–0.6858	5.99	
10.0333–0.2000	7	3	6.1	10.0629	–0.1675	7.84	
10.0750–0.4167	4	10	9.7	10.0701	–0.4180	3.53	
10.1750–0.3667	10	40	220.6	10.1502	–0.3447	79.6	
10.1833–0.0139	9	5	4.4	10.1835	–0.0125	8.70	
10.2306–0.3042	3	15	12.1	10.2291	–0.2959	1.97	
10.2375–0.0792	4	5	4.7	10.2463	–0.0770	2.38	
10.2611+0.0750	2	5	5.1	10.2630	+0.0758	0.721	
10.3139–0.1417	4	80	220.5	10.3008	–0.1475	17.8	
10.3208–0.2611	1	25	29.0	10.3213	–0.2586	0.474	
10.4500+0.0167	4	20	114.0	10.4619	+0.0341	3.57	
10.5861–0.0417	6	2	2.4	10.5864	–0.0243	3.22	
10.6333–0.4000	10	15	261.4	10.6236	–0.3840	14.5	
10.6917+0.0333	5	3	5.5	10.7026	+0.0257	2.32	
10.8556–0.1250	3	3	2.3	10.8549	–0.1243	0.56	
10.8750+0.0875	6	4	4.9	10.8950	+0.0640	4.05	
10.9639+0.0167	2	12	55.7	10.9650	+0.0096	1.10	
11.0000–0.0528	8	5	6.7	11.0384	–0.0393	5.53	
11.0333+0.0639	2	15	51.1	11.0339	+0.0629	0.595	
11.0736–0.2264	1	5	2.8	11.0756	–0.2282	0.135	
11.1639–0.7167	10	2	1.9	11.1166	–0.6535	3.11	
11.1833–0.3500	6	35	51.2	11.1778	–0.3752	23.1	SNR G11.2-0.3
11.2000+0.1167	10	5	8.3	11.2468	+0.0691	10.8	
11.3889–0.0667	9	10	75.4	11.3440	–0.0381	13.6	SNR G11.4-0.1

TABLE 3 — *Continued*

Name ° (1)	Box Size arcmin (2)	Scale mJy/beam (3)	S_p mJy/beam (4)	l_p ° (5)	b_p ° (6)	S_i Jy (7)	Comment (8)
11.5500+0.3333	10	2	2.5	11.5174	+0.3541	4.34	
11.7708−0.0375	1	9	9.7	11.7730	−0.0409	0.247	
11.8000−0.1083	8	2	63.9	11.8369	−0.1736	5.16	
11.8903−0.2250	6	2	4.2	11.8753	−0.2370	3.03	
11.8917+0.7500	5	10	11.8	11.9113	+0.7464	4.20	
11.9500−0.0889	10	10	190.0	11.9447	−0.0364	12.6	SNR G12.0+0.1
11.9694+0.1917	2	30	51.6	11.9686	+0.1814	1.27	
11.9903−0.2458	6	5	4.6	12.0003	−0.2542	2.99	
12.0639−0.2819	1	3	3.1	12.0647	−0.2842	0.10	
12.2083−0.1167	4	15	88.3	12.2081	−0.1020	5.20	
12.2694+0.2972	6	3	2.8	12.2759	+0.2642	2.62	
12.3167+0.4250	4	2	3.2	12.3164	+0.4292	0.969	
12.4167+0.4667	7	2	5.4	12.4181	+0.5036	2.28	
12.4361−0.0417	4	4	37.2	12.4298	−0.0481	2.52	
12.5125−0.1056	4	2	2.7	12.5070	−0.0969	1.71	
12.7167+0.0000	8	6	7.0	12.6814	+0.0058	8.56	
12.7500+0.3333	4	2	6.9	12.7759	+0.3336	1.51	
12.8000−0.1833	16	25	423.2	12.8059	−0.2003	68.0	
12.8208−0.0208	4	4	5.1	12.8198	−0.0342	3.40	
12.8222+0.5417	3	2	13.3	12.8159	+0.5575	0.331	
12.9139−0.2806	3	15	16.4	12.9142	−0.2814	1.39	
13.1875+0.0389	4.5	20	27.0	13.1831	+0.0514	7.58	
13.2119+0.1411	2	10	1.9	13.2209	+0.1247	0.26	
13.2306+0.0819	2.5	5	5.4	13.2336	+0.0758	1.25	
13.4500+0.1389	6	8	10.3	13.4559	+0.1747	9.15	SNR G13.5+0.2
13.5389−0.1861	8	3	24.6	13.5420	−0.1820	6.26	
13.7083−0.2417	2	3	2.6	13.7065	−0.2436	0.359	
13.8042+0.1833	4	3	3.4	13.8098	+0.1847	1.84	
13.8750+0.2819	2.5	75	212.5	13.8726	+0.2819	4.42	
13.8875−0.4778	2	5	4.6	13.8921	−0.4752	0.32	
13.8986−0.0153	2	8	9.2	13.8970	−0.0175	0.65	
13.9931−0.1278	4	10	11.1	13.9880	−0.1332	4.64	
14.1028+0.0917	2	15	36.9	14.1048	+0.0918	0.506	
14.1111−0.1500	12	5	16.9	14.2059	−0.1104	25.2	
14.2208−0.3083	7	3	9.8	14.2665	−0.2718	9.57	
14.2300−0.5000	28	3	53.1	14.3832	−0.5146	73.0	
14.3250+0.1333	4	5	3.6	14.3316	+0.1329	1.91	
14.3625−0.1694	7	4	3.5	14.3494	−0.1510	8.57	
14.4292−0.0639	4	5	5.0	14.4144	−0.0726	3.43	
14.6167+0.0667	14	8	9.7	14.5989	+0.0202	37.6	
15.0667−0.6833	18	400	418.7	15.0340	−0.6786	738	
15.0764−0.1222	2	25	13.0	15.0763	−0.1209	0.436	
15.4350+0.1600	15	3	5.8	15.5197	+0.1903	8.81	
15.8917+0.1917	7.5	15	14.3	15.9135	+0.1842	6.54	SNR G15.9+0.2
15.9583+0.7167	9	2	1.7	15.9146	+0.7447	0.42	
16.2458+0.0389	2	2	1.7	16.2436	+0.0419	0.231	
16.2917−0.1667	6	5	6.2	16.3019	−0.1497	4.06	
16.3583−0.1833	4	4	7.9	16.3603	−0.2081	2.48	
16.4306−0.2000	3	10	9.9	16.4442	−0.1953	1.88	
16.6500−0.3333	12	4	11.8	16.6002	−0.2758	12.6	
16.7417+0.0833	6	8	10.3	16.7431	+0.0892	5.12	SNR G16.7+0.1
16.9417+0.7333	15	20	26.2	16.9508	+0.7825	47.9	
17.0167−0.0333	8	4	4.5	16.9603	−0.0869	2.63	
17.0917−0.1111	6	3	13.4	17.1142	−0.1125	2.81	
17.2903−0.2022	1	12	10.0	17.2875	−0.1997	0.24	
17.3361−0.1389	3	3	2.9	17.3358	−0.1397	0.282	
17.3625−0.0375	1.5	7	7.7	17.3636	−0.0369	0.30	
17.4458−0.0750	3	3	2.4	17.4486	−0.0625	0.717	
17.5167−0.1125	9	2	3.8	17.5614	−0.1069	2.61	
17.5861+0.0917	2	2	2.1	17.5847	+0.0919	0.29	
17.6250+0.0472	1	2	1.8	17.6270	+0.0458	0.069	
17.9278−0.6778	2	3	2.5	17.9298	−0.6758	0.185	
18.0778+0.0708	2	6	6.2	18.0792	+0.0708	0.474	
18.0972−0.3208	1.5	4	4.0	18.0931	−0.3186	0.19	
18.1408−0.2806	4	50	83.0	18.1465	−0.2831	8.89	
18.1500−0.1722	9	8	7.8	18.1915	−0.1725	9.69	
18.1500+0.1000	3	1	2.0	18.1615	+0.0897	0.563	
18.1889−0.3972	6	5	6.4	18.1853	−0.3703	7.27	
18.2333−0.2361	6	8	10.1	18.2610	−0.2853	7.57	
18.2536−0.3083	5	12	15.8	18.2748	−0.2903	8.51	
18.3028−0.3894	1	175	174.8	18.3031	−0.3892	1.71	
18.3292+0.0167	5	1	2.1	18.3176	+0.0286	1.72	
18.3861−0.3861	3	1.5	2.0	18.3887	−0.3742	0.925	
18.4417+0.0131	1	7	6.2	18.4410	+0.0136	0.114	
18.4531−0.0081	2	15	87.4	18.4615	−0.0036	0.71	

TABLE 3 — *Continued*

Name ($l+b$) ° (1)	Box Size arcmin (2)	Scale mJy/beam (3)	S_p mJy/beam (4)	l_p ° (5)	b_p ° (6)	S_i Jy (7)	Comment (8)
18.5181+0.3000	14	3	97.1	18.4944	+0.2731	6.96	
18.6375−0.2917	6	4	4.1	18.6077	−0.3153	4.31	
18.6556−0.0569	1.5	8	9.7	18.6561	−0.0581	0.275	
18.6778−0.2347	1.5	15	25.8	18.6733	−0.2364	0.625	
18.7361−0.1903	1	3	3.0	18.7356	−0.1886	0.173	
18.7583−0.0736	3	9	10.2	18.7600	−0.0708	1.34	
18.7639−0.1667	3	3	3.4	18.7600	−0.1636	1.26	
18.7736+0.4000	18	8	22.0	18.7611	+0.2631	41.4	SNR G18.8+0.3 (Kes 67)
18.8667−0.2667	34	15	130.8	18.6970	−0.4008	158	
19.0500−0.5861	5	7	12.0	19.0919	−0.5874	2.86	
19.2742+0.5444	1	1.5	1.2	19.2747	+0.5442	0.054	
19.4611+0.1444	9	7	105.9	19.4917	+0.1353	8.09	
19.5917+0.0250	1.5	3	2.9	19.5923	+0.0292	0.245	
19.6000−0.2000	15	7	306.6	19.6107	−0.2342	24.7	
19.6639−0.3042	2	3	2.5	19.6663	−0.2992	0.221	
19.7139−0.2583	1.5	3	2.1	19.7130	−0.2564	0.224	
19.7417+0.2800	1	25	31.2	19.7402	+0.2814	0.298	
19.7600−0.5500	12	2	10.3	19.7522	−0.5291	7.46	
19.7833+0.2833	3	3	2.9	19.7836	+0.2869	0.694	
19.8111+0.0139	4	1.5	1.7	19.8025	+0.0264	1.06	
19.9375+0.5194	1	5	7.1	19.9364	+0.5208	0.029	
19.9653+0.0800	1	2	2.3	19.9676	+0.0858	0.045	
19.9833−0.1833	13	6	9.8	19.9537	−0.2497	19.0	SNR G20.0-0.2
20.0764−0.1389	1	75	98.4	20.0721	−0.1419	0.863	
20.0975−0.1214	1	10	8.7	20.0994	−0.1231	0.12	
20.1806+0.0778	15	1.5	2.8	20.1299	+0.1986	7.57	
20.2222+0.1106	2	2	2.1	20.2217	+0.1114	0.252	
20.3561−0.0444	1	2	1.3	20.3567	−0.0447	0.047	
20.3853−0.0208	1.5	2	1.8	20.3828	−0.0197	0.128	
20.4583+0.0056	6	1.5	3.9	20.4957	+0.0431	2.04	
20.4667+0.1500	9	3	4.6	20.4095	+0.0997	6.56	
20.7333−0.1333	14	12	30.9	20.7510	−0.0899	24.1	
20.9725−0.0711	1	2	10.7	20.9639	−0.0743	0.079	
20.9917+0.0903	3	20	27.1	20.9883	+0.0896	1.69	
21.0269−0.4719	10	1	1.5	21.0216	−0.4430	2.32	
21.0417−0.2486	6	1	3.4	21.0600	−0.2354	1.51	
21.1500−0.3000	8	3	2.2	21.1328	−0.3057	3.20	
21.2486+0.0556	2	2	1.3	21.2490	+0.0558	0.097	
21.3444−0.1375	1	2	1.8	21.3435	−0.1376	0.066	
21.4619−0.5903	4	2.5	3.0	21.4557	−0.5886	0.816	
21.5569−0.1028	6	1	1.5	21.5430	−0.1037	1.90	
21.6417+0.0000	5	2	5.4	21.6319	−0.0070	1.54	
21.6806−0.2333	10	2	19.7	21.6036	−0.1681	5.15	
21.7078+0.0972	6	2	17.5	21.7514	+0.1308	1.98	
21.8167−0.5000	24	20	27.3	21.8202	−0.4775	98.6	SNR G21.8-0.6 (Kes 69)
21.8731+0.0064	2	20	152.8	21.8747	+0.0080	1.29	
21.9300+0.1014	1.5	2	2.1	21.9331	+0.1003	0.21	
21.9764+0.0458	2	2	2.2	21.9753	+0.0486	0.42	
22.0528−0.0167	15	1.5	6.4	22.0964	+0.0080	13.2	
22.2767−0.0944	3	1.5	1.6	22.2575	−0.0986	0.844	
22.3069−0.0569	2	2	2.8	22.3036	−0.0620	0.439	
22.3833+0.1000	8	2	5.5	22.3597	+0.0647	4.66	
22.7333−0.2000	30	7	61.1	22.9364	−0.0736	130	SNR G22.7-0.2
22.7486−0.2458	4	7	6.6	22.7603	−0.2447	3.65	
22.7583−0.4917	5	12	20.8	22.7592	−0.4775	6.01	
22.9917−0.3583	4.5	7	15.2	22.9742	−0.3919	5.10	
23.0100+0.2650	9	1.5	5.0	23.0209	+0.1903	5.24	
23.1069+0.5500	9	3	25.4	23.0675	+0.5186	6.25	
23.2417−0.3333	30	20	45.5	23.2937	−0.2775	122	SNR G23.3-0.3 (W41)
23.2556+0.2917	1.7	2	2.4	23.2559	+0.2930	0.334	
23.3750+0.4500	2	3	3.0	23.3803	+0.4508	0.35	
23.4167−0.2000	10	25	30.0	23.4359	−0.2086	26.1	
23.5500+0.2833	16	3	3.2	23.5392	+0.3214	20.3	SNR G23.6+0.3
23.5667−0.0333	13	7	9.0	23.5426	−0.0397	23.3	
23.6583−0.2500	2	6	5.6	23.6581	−0.2520	0.501	
23.6639+0.4806	4	2	2.1	23.6848	+0.4947	0.973	
23.7000−0.2000	3	7	10.7	23.7031	−0.1959	1.36	
23.7042+0.1722	2	50	136.3	23.7109	+0.1708	2.54	
23.7417−0.0167	2	3	5.7	23.7404	−0.0159	0.329	
23.7944+0.2333	7	4	4.9	23.8265	+0.2186	3.75	
23.8167+0.3917	3	2	2.1	23.8121	+0.3814	0.779	
23.8361+0.1042	2	9	8.3	23.8354	+0.1036	0.571	
23.8667−0.1167	3	20	51.2	23.8704	−0.1225	2.31	
23.9000+0.0667	2	9	56.4	23.8982	+0.0647	0.745	
23.9569+0.1528	3	15	206.7	23.9565	+0.1497	3.05	

TABLE 3 — *Continued*

Name $(l+b)$ (1)	Box Size arcmin (2)	Scale mJy/beam (3)	S_p mJy/beam (4)	l_p (5)	b_p (6)	S_i Jy (7)	Comment (8)
23.9875−0.1000	2	6	20.8	23.9875	−0.0893	0.756	
24.0222+0.1917	1	2	2.1	24.0225	+0.1934	0.106	
24.1200−0.0694	3	3	3.3	24.1320	−0.0754	1.58	
24.1300+0.4500	6	2	2.5	24.1325	+0.4518	1.75	
24.1417+0.1236	3	9	72.0	24.1198	+0.1262	1.30	
24.1803+0.2167	7	3	44.5	24.1470	+0.1746	5.39	
24.1969+0.2444	1	7	7.4	24.1981	+0.2424	0.243	
24.3000−0.1350	10	5	22.0	24.3366	−0.1576	17.8	
24.3806+0.0750	7	7	12.3	24.4027	+0.0685	10.9	
24.3958+0.5778	5	2	2.9	24.3637	+0.5746	2.38	
24.4750+0.4917	5	25	98.2	24.4721	+0.4880	8.37	
24.5000−0.0417	5	5	86.4	24.4922	−0.0387	5.62	
24.5083−0.2333	9	7	105.8	24.5072	−0.2221	17.1	
24.5083+0.2333	12	10	92.2	24.4638	+0.2463	29.9	
24.5583−0.1333	2	4	4.4	24.5417	−0.1376	0.888	
24.6667+0.6000	18	4	235.5	24.5410	+0.5996	38.7	SNR G24.7+0.6
24.6819−0.1625	3	25	46.8	24.6756	−0.1537	4.77	
24.7083−0.6333	18	8	16.3	24.7533	−0.7241	21.7	SNR G24.7−0.6
24.7167−0.0861	7	8	24.3	24.7106	−0.1265	12.8	
24.7319+0.1569	2	5	3.6	24.7356	+0.1524	0.763	
24.7383+0.0778	3	6	7.0	24.7534	+0.0624	2.39	
24.7417−0.2083	3	8	11.8	24.7462	−0.2037	2.42	
24.7931+0.0972	1.5	60	83.6	24.7984	+0.0963	2.54	
24.8250+0.0917	7	15	40.8	24.8496	+0.0880	14.7	
24.8319−0.1014	3	3	2.6	24.8384	−0.1065	1.10	
24.9528−0.0472	2	3	3.1	24.9574	−0.0520	0.575	
25.1417−0.3403	3	2	6.9	25.1568	−0.3275	0.526	
25.1500+0.0764	4	8	11.6	25.1530	+0.0891	2.34	
25.2222+0.2917	3	2.5	3.2	25.2185	+0.2875	1.42	
25.2472−0.1417	3	50	579.0	25.2663	−0.1609	3.26	
25.2667−0.3167	6	4	5.8	25.2535	−0.3225	6.19	
25.2917+0.3083	5	4	4.9	25.2880	+0.3152	4.27	
25.3806−0.1750	7	40	331.2	25.3980	−0.1414	24.6	
25.3833−0.3500	8	3	4.3	25.3680	−0.3653	8.39	
25.3986+0.0292	1.5	25	179.8	25.3947	+0.0330	1.29	
25.4042−0.2542	4	7	7.9	25.4024	−0.2536	2.41	
25.4597−0.2083	1	30	46.8	25.4597	−0.2086	0.362	
25.4694−0.1250	3	4	3.9	25.4713	−0.1170	1.22	
25.4750+0.0403	3	2	2.7	25.4763	+0.0458	1.12	
25.5389+0.2236	2	3	5.5	25.5225	+0.2162	0.533	
25.6167−0.4597	4	2	2.9	25.6192	−0.4262	1.17	
25.6528−0.0333	4	3	2.6	25.6554	−0.0332	2.12	
25.6611−0.0167	1	3.5	3.7	25.6626	−0.0182	0.197	
25.7056+0.0389	3.5	15	16.9	25.7160	+0.0485	4.17	
25.8700+0.1350	19	5	102.8	25.7882	+0.0768	59.6	
26.1000−0.0917	9	8	48.0	26.0906	−0.0576	12.6	
26.1292+0.0083	7	5	17.7	26.0823	−0.0348	8.31	
26.2611+0.2819	2	2	2.1	26.2618	+0.2735	0.41	
26.3181−0.0111	1	9	12.1	26.3163	−0.0115	0.249	
26.3292−0.0708	2	4	4.6	26.3296	−0.0737	0.631	
26.4333+0.6083	5	3	4.9	26.4301	+0.6452	1.45	
26.4708+0.0208	3	7	19.5	26.4702	+0.0213	1.12	
26.5333+0.1833	4	2	2.3	26.5363	+0.1852	1.97	
26.5375+0.4167	5	10	113.1	26.5446	+0.4152	3.67	
26.5500+0.0583	5	2	25.2	26.5358	+0.0252	2.68	
26.5542−0.3083	12	3	96.4	26.6091	−0.2119	15.1	
26.5931+0.0944	1	7	8.0	26.5880	+0.0963	0.322	
26.5972−0.0236	2	5	50.9	26.5974	−0.0237	0.697	
26.6083−0.0917	8	2	8.9	26.6413	−0.0387	9.91	
26.6444+0.0194	1	7	7.8	26.6452	+0.0197	0.199	
26.6667−0.2000	6	2	2.6	26.6280	−0.1537	4.79	
26.7208+0.1722	2	10	11.3	26.7197	+0.1736	0.584	
26.8222+0.3778	3	2	3.4	26.8180	+0.3891	0.612	
26.8667−0.2750	2	3	2.5	26.8675	−0.2714	0.529	
26.9458+0.2083	4	3	2.0	26.9658	+0.2336	1.03	
26.9500+0.0708	10	3	6.1	26.9697	+0.0219	8.22	
26.9833−0.0500	6	5	6.3	26.9736	−0.0709	5.97	
27.1333+0.0333	11	5	5.7	27.1420	−0.0125	17.8	
27.1750−0.0708	3	4	21.5	27.1859	−0.0814	1.70	
27.1875−0.1542	2	4	4.9	27.1897	−0.1497	0.884	
27.2792+0.1514	3	12	177.6	27.2797	+0.1447	2.37	
27.2903−0.6486	1	2	1.8	27.2919	−0.6486	0.03	
27.3167−0.1250	7	8	33.9	27.3642	−0.1658	6.36	
27.3375+0.1778	3	3	3.3	27.3331	+0.1725	1.35	
27.3542−0.0833	6	3	10.4	27.3164	−0.1331	3.97	

TABLE 3 — *Continued*

Name ($l+b$) ° (1)	Box Size arcmin (2)	Scale mJy/beam (3)	S_p mJy/beam (4)	l_p ° (5)	b_p ° (6)	S_i Jy (7)	Comment (8)
27.3750+0.6542	3	2	1.8	27.3725	+0.6564	0.517	
27.3917−0.0111	6	13	19.8	27.3664	+0.0153	10.1	SNR G27.4+0.0 (4C-004.71)
27.5000+0.1861	6	10	39.2	27.4942	+0.1897	7.71	
27.5000+0.6500	10	2.5	3.0	27.5375	+0.6725	5.74	
27.6833+0.0778	3	2	1.6	27.6820	+0.0881	0.432	
27.7139+0.5833	34	2	94.9	27.7020	+0.7047	54.0	SNR G27.8+0.6
27.8042−0.3000	6	2	7.9	27.7609	−0.3403	1.12	
27.9319+0.2056	1	11	11.9	27.9331	+0.2058	0.154	
28.0125+0.3194	5	2	8.5	27.9781	+0.3603	1.55	
28.0208−0.0417	7	4	8.9	28.0314	−0.0725	6.67	
28.1278+0.3403	2	4	3.6	28.1270	+0.3408	0.21	
28.1500+0.1583	3	2.5	2.7	28.1514	+0.1631	0.993	
28.3028−0.3889	2	24	24.1	28.3053	−0.3853	1.17	
28.3194−0.0222	2	4	3.8	28.3186	−0.0125	0.868	
28.3750+0.2028	12	2	11.4	28.3470	+0.1736	14.9	
28.4333−0.0056	3.5	5	38.1	28.4514	+0.0025	2.37	
28.5167+0.1333	10	2	26.6	28.5814	+0.1453	13.0	
28.5167+0.3000	3	3	2.6	28.5259	+0.2980	1.34	
28.5583−0.0083	4.5	10	17.5	28.5687	+0.0203	5.37	
28.5972−0.3639	2.5	12	15.6	28.5948	−0.3591	1.21	
28.6111+0.0139	1	20	115.5	28.6087	+0.0186	0.81	
28.6111−0.1167	10	10	36.3	28.6103	−0.1414	17.7	SNR G28.6-0.1
28.6333+0.1917	6	4	8.4	28.5831	+0.1453	5.16	
28.6361+0.4806	2	6	6.9	28.6354	+0.4769	0.791	
28.6514+0.0292	4	8	124.9	28.6520	+0.0275	4.71	
28.6958+0.0458	3	10	13.4	28.7026	+0.0430	3.26	
28.7292−0.2333	2	2	2.1	28.7281	−0.2309	0.374	
28.7653+0.2750	3	5	3.7	28.7687	+0.2741	1.48	
28.7667−0.4250	13	2	5.4	28.7698	−0.4264	10.9	
28.7972+0.2444	3	7	11.4	28.7881	+0.2430	2.16	
28.8000+0.1764	2	35	46.3	28.8070	+0.1752	2.87	
28.8278−0.2278	4	5	5.9	28.8370	−0.2509	2.89	
28.8619+0.0625	2	3	3.1	28.8615	+0.0652	0.765	
28.9000+0.2417	4	2	2.4	28.9021	+0.2402	1.98	
28.9833−0.6042	4	4	3.5	28.9727	−0.6219	2.13	
29.0028+0.0861	4	4	5.8	29.0032	+0.0702	2.65	
29.0167+0.1722	3	3	5.2	28.9982	+0.1897	1.00	
29.0667−0.6750	10	2	46.1	29.0444	−0.5986	7.56	
29.0778+0.4542	2	8	8.1	29.0771	+0.4586	0.657	
29.1333+0.4333	8	3	3.9	29.1271	+0.4363	7.09	
29.1333−0.1458	1	4	3.9	29.1343	−0.1487	0.141	
29.1583−0.0500	10	3	91.7	29.2110	−0.0687	13.3	
29.2444+0.4431	4	2	2.4	29.2366	+0.4569	1.28	
29.3667+0.1000	12	4	6.5	29.3711	+0.1035	16.6	
29.5667+0.1083	7	2	3.0	29.6156	+0.0757	4.27	SNR G29.6+0.1
29.6181−0.5972	1	2	1.5	29.6185	−0.5968	0.05	
29.7083−0.2417	4	35	104.4	29.6890	−0.2421	10.7	SNR G29.7-0.3 (Kes 75)
29.9333−0.0667	15	10	355.6	29.9563	−0.0175	46.8	
29.9792−0.6056	3	2	1.8	29.9757	−0.6069	0.909	
30.0542−0.3389	2.5	4	3.7	30.0563	−0.3403	1.12	
30.2083−0.1667	4	6	503.0	30.2335	−0.1381	4.91	
30.2486+0.2431	1.5	7	9.9	30.2468	+0.2447	0.347	
30.2583−0.0250	4	5	6.5	30.2496	−0.0192	3.55	
30.3194−0.2083	3	3	3.8	30.3357	−0.2064	1.54	
30.3667−0.2583	9	7	10.8	30.4374	−0.2064	12.7	
30.3750+0.0250	2.5	5	5.7	30.3769	+0.0219	1.06	
30.3778+0.1097	1	6	6.9	30.3785	+0.1075	0.177	
30.3819−0.1097	1	8	13.7	30.3830	−0.1108	0.315	
30.4583+0.4333	7	2	5.6	30.4707	+0.4736	4.28	
30.5083−0.3292	7	5	5.0	30.5102	−0.2997	8.26	
30.5333+0.0208	1.5	15	199.7	30.5346	+0.0208	1.56	
30.5583−0.5000	12	4	47.5	30.5363	−0.4436	17.2	
30.7050−0.2750	4.5	20	34.7	30.6874	−0.2608	7.43	
30.7500−0.0500	13	50	267.1	30.7196	−0.0825	142	
30.7667−0.2250	3	6	8.9	30.7691	−0.2197	2.62	
30.7958+0.1653	1	10	12.6	30.7974	+0.1686	0.376	
30.8333−0.2069	5	6	7.8	30.8541	−0.1931	5.67	
30.8486+0.1333	4	10	90.4	30.8663	+0.1142	3.81	
30.8903+0.1764	1	3	2.7	30.8908	+0.1753	0.189	
30.9069+0.1611	1	4	4.3	30.9063	+0.1625	0.209	
30.9500+0.5417	2	7	7.2	30.9513	+0.5397	0.60	
30.9569+0.0819	1	20	36.2	30.9580	+0.0869	0.526	
30.9639+0.5917	4	4	4.6	30.9519	+0.5919	2.09	
31.0000−0.0500	6	4	4.4	31.0252	−0.0653	7.34	
31.0083+0.5500	5	2	1.9	31.0447	+0.5081	1.92	

TABLE 3 — *Continued*

Name $(l+b)$ °	Box Size arcmin	Scale mJy/beam	S_p mJy/beam	l_p °	b_p °	S_i Jy	Comment
(1)	(2)	(3)	(4)	(5)	(6)	(7)	(8)
31.0500+0.0833	3	10	17.8	31.0596	+0.0919	3.17	
31.0583+0.4833	6	5	11.6	31.0497	+0.4697	4.86	
31.0653+0.0444	2	10	83.2	31.0702	+0.0508	1.44	
31.0708−0.0444	2	4	4.9	31.0741	−0.0458	1.21	
31.0786+0.0236	1.5	4	4.1	31.0774	+0.0247	0.636	
31.1217+0.0486	3	4	6.4	31.1219	+0.0631	2.44	
31.1319+0.2889	4	6	8.3	31.1308	+0.2686	2.90	
31.1750−0.1083	7	4	15.7	31.1874	−0.0647	7.50	
31.2486−0.0278	6	3	3.8	31.2596	−0.0231	5.81	
31.2736+0.4778	3	2	1.6	31.2669	+0.4886	0.556	
31.2972+0.0500	3	3	99.1	31.2796	+0.0631	1.76	
31.3708−0.0361	3	3	2.6	31.3702	−0.0464	1.17	
31.4000−0.2667	3	15	36.0	31.3947	−0.2592	2.31	
31.4667−0.3444	3	9	9.9	31.4758	−0.3453	1.24	
31.4903+0.3708	1	4	2.6	31.4913	+0.3680	0.12	
31.5417−0.1056	3	2	2.0	31.5402	−0.1070	0.772	
31.5500−0.7167	22	2	20.5	31.3725	−0.7514	7.65	SNR G31.5-0.6
31.6097+0.3347	4.5	3	3.7	31.6219	+0.3319	1.74	
31.6125−0.2389	4	2	2.2	31.6258	−0.2436	1.31	
31.7278+0.7000	1	2	1.8	31.7270	+0.6975	0.057	
31.8208−0.1222	3	3	3.2	31.8241	−0.1136	0.896	
31.8667+0.0111	8	25	73.2	31.8680	+0.0641	27.6	SNR G31.9+0.0 (3C391)
31.9069−0.3083	1	3	3.0	31.9053	−0.3081	0.076	
31.9417+0.1778	5	2	7.4	31.9097	+0.1952	1.19	

TABLE 4
HIGH-PROBABILITY SUPERNOVA REMNANT CANDIDATES

Name ($l+b$) °	Diameter arcmin	Box Size arcmin	S_p mJy/beam	S_i Jy
(1)	(2)	(3)	(4)	(5)
6.4500–0.5583	3.3	6.0	4.7	6.64
6.5375–0.6028	5.0	9.0	16.9	9.42
7.2167+0.1833	6.5	10.0	17.2	9.10
8.3083–0.0861	3.0	6.0	263.5	7.00
8.8583–0.2583	4.0	6.0	3.4	4.79
9.6833–0.0667	8.5	12.0	7.2	12.5
10.8750+0.0875	2.8	6.0	4.9	4.05
11.1639–0.7167	7.0	10.0	1.9	3.11
11.2000+0.1167	7.5	10.0	8.3	10.8
11.5500+0.3333	4.5	10.0	2.5	4.34
11.8903–0.2250	3.5	6.0	4.2	3.03
12.2694+0.2972	4.0	6.0	2.8	2.62
12.7167+0.0000	4.5	8.0	7.0	8.56
12.8208–0.0208	2.0	4.0	5.1	3.40
12.9139–0.2806	1.5	3.0	16.4	1.39
13.1875+0.0389	2.5	4.5	27.0	7.58
16.3583–0.1833	2.8	4.0	7.9	2.48
17.0167–0.0333	4.0	8.0	4.5	2.63
17.3361–0.1389	1.8	3.0	2.9	0.282
18.1500–0.1722	7.0	9.0	7.8	9.69
18.2536–0.3083	3.5	5.0	15.8	8.51
18.6375–0.2917	4.0	6.0	4.1	4.31
18.7583–0.0736	1.6	3.0	10.2	1.34
19.4611+0.1444	6.0	9.0	105.9	8.09
19.5800–0.2400	3.2	5.0	306.6	6.61
19.5917+0.0250	0.8	1.5	2.9	0.245
19.6100–0.1200	4.5	6.0	8.5	5.87
19.6600–0.2200	4.5	6.0	10.2	4.80
20.4667+0.1500	5.5	9.0	4.6	6.56
21.5569–0.1028	4.0	6.0	1.5	1.90
21.6417+0.0000	2.8	5.0	5.4	1.54
22.3833+0.1000	7.0	8.0	5.5	4.66
22.7583–0.4917	3.8	5.0	20.8	6.01
22.9917–0.3583	3.8	4.5	15.2	5.10
23.5667–0.0333	9.0	13.0	9.0	23.3
24.1803+0.2167	5.2	7.0	44.5	5.39
25.2222+0.2917	2.0	3.0	3.2	1.42
27.1333+0.0333	11.0	11.0	5.7	17.8
28.3750+0.2028	10.0	12.0	11.4	14.9
28.5167+0.1333	14.0	10.0	26.6	13.0
28.5583–0.0083	3.0	4.5	17.5	5.37
28.7667–0.4250	9.5	13.0	5.4	10.9
29.0667–0.6750	8.0	10.0	46.1	7.56
29.0778+0.4542	0.7	2.0	8.1	0.657
29.3667+0.1000	9.0	12.0	6.5	16.6
30.8486+0.1333	2.2	4.0	90.4	3.81
31.0583+0.4833	4.5	6.0	11.6	4.86
31.6097+0.3347	3.1	4.5	3.7	1.74
31.8208–0.1222	1.8	3.0	3.2	0.896